NOAA Technical Report NWS 22

The Nested Grid Model

Silver Spring, Md.
April 1979

U.S. DEPARTMENT OF COMMERCE
National Oceanic and Atmospheric Administration
National Weather Service

NOAA TECHNICAL REPORTS

National Weather Service Series

The National Weather Service (NWS) observes and measures atmospheric phenomena; develops and distributes forecasts of weather conditions and warnings of adverse weather; collects and disseminates weather information to meet the needs of the public and specialized users. The NWS develops the national meteorological service system and improves procedures, techniques, and dissemination for weather and hydrologic measurements, and forecasts.

NWS series of NOAA Technical Reports is a continuation of the former series, ESSA Technical Report Weather Bureau (WB).

Reports listed below are available from the National Technical Information Service, U.S. Department of Commerce, Sills Bldg., 5285 Port Royal Road, Springfield, Va. 22161. Prices vary. Order by accession number (given in parentheses).

ESSA Technical Reports

WB 1 Monthly Mean 100-, 50-, 30-, and 10-Millibar Charts January 1964 through December 1965 of the IQSY Period. Staff, Upper Air Branch, National Meteorological Center, February 1967, 7 p, 96 charts. (AD 651 101)

WB 2 Weekly Synoptic Analyses, 5-, 2-, and 0.4-Mb Surfaces for 1964 (based on observations of the Meteorological Rocket Network during the IQSY). Staff, Upper Air Branch, National Meteorological Center, April 1967, 16 p, 160 charts. (AD 652 696)

WB 3 Weekly Synoptic Analyses, 5-, 2-, and 0.4-Mb Surfaces for 1965 (based on observations of the Meteorological Rocket Network during the IQSY). Staff, Upper Air Branch, National Meteorological Center, August 1967, 173 p. (AD 662 053)

WB 4 The March-May 1965 Floods in the Upper Mississippi, Missouri, and Red River of the North Basins. J. L. H. Paulhus and E. R. Nelson, Office of Hydrology, August 1967, 100 p.

WB 5 Climatological Probabilities of Precipitation for the Conterminous United States. Donald L. Jorgensen, Techniques Development Laboratory, December 1967, 60 p.

WB 6 Climatology of Atlantic Tropical Storms and Hurricanes. M. A. Alaka, Techniques Development Laboratory, May 1968, 18 p.

WB 7 Frequency and Areal Distributions of Tropical Storm Rainfall in the United States Coastal Region on the Gulf of Mexico. Hugo V. Goodyear, Office of Hydrology, July 1968, 33 p.

WB 8 Critical Fire Weather Patterns in the Conterminous United States. Mark J. Schroeder, Weather Bureau, January 1969, 31 p.

WB 9 Weekly Synoptic Analyses, 5-, 2-, and 0.4-Mb Surfaces for 1966 (based on meteorological rocketsonde and high-level rawinsonde observations). Staff, Upper Air Branch, National Meteorological Center, January 1969, 169 p.

WB 10 Hemispheric Teleconnections of Mean Circulation Anomalies at 700 Millibars. James F. O'Connor, National Meteorological Center, February 1969, 103 p.

WB 11 Monthly Mean 100-, 50-, 30-, and 10-Millibar Charts and Standard Deviation Maps, 1966-1967. Staff, Upper Air Branch, National Meteorological Center, April 1969, 124 p.

WB 12 Weekly Synoptic Analyses, 5-, 2-, and 0.4-Millibar Surfaces for 1967. Staff, Upper Air Branch, National Meteorological Center, January 1970, 169 p.

NOAA Technical Reports

NWS 13 The March-April 1969 Snowmelt Floods in the Red River of the North, Upper Mississippi, and Missouri Basins. Joseph L. H. Paulhus, Office of Hydrology, October 1970, 92 p. (COM-71-50269)

NWS 14 Weekly Synoptic Analyses, 5-, 2-, and 0.4-Millibar Surfaces for 1968. Staff, Upper Air Branch, National Meteorological Center, May 1971, 169 p. (COM-71-50383)

NWS 15 Some Climatological Characteristics of Hurricanes and Tropical Storms, Gulf and East Coasts of the United States. Francis P. Ho, Richard W. Schwerdt, and Hugo V. Goodyear, May 1975, 87 p. (COM-75-11088)

(Continued on inside back cover)

NOAA Technical Report NWS 22

The Nested Grid Model

Norman A. Phillips

National Meteorological Center
Silver Spring, Md.
April 1979

DEPARTMENT OF COMMERCE
Juanita M. Kreps, Secretary

National Oceanic and Atmospheric Administration
Richard A. Frank, Administrator

National Weather Service
Richard E. Hallgren, Director

ACKNOWLEDGMENTS

Kenneth Campana has been an invaluable advisor and collaborator in programming, coding, and running the Nested Grid Model (NGM). Without his enthusiastic and experienced participation, this model would be in a much less satisfactory state. Mukut Mathur has also helped greatly by assuming responsibility for the preparation of the orography, roughness, and ocean temperature fields.

John Stackpole's advice on the dry-adiabatic adjustment was helpful, as was a description of their implementation of the Kuo convection given by John Hovermale and Robert Livezey. David Parrish supplied a program to generate a convenient input GLOPEP tape from the Flattery analysis. Kikuro Miyakoda and Eric Pitcher contributed fine-resolution ground heights over the United States and a high-order spherical harmonic program for the orography field used in the NGM. Peter Chase, Armand Desmarais, Willette Carlton, and James Howcroft provided excellent advice on occasional questions of coding tactics and system strategy. John Brown, Joseph Gerrity, John Hovermale, and Frederick Shuman have participated in many discussions about various aspects of the model and suggestions for its application to important forecast problems at NMC.

Mary Daigle has contributed very effectively by her skillful preparation of this manuscript, as well as earlier documentation and NMC Office Notes associated with this model.

The support of Martha Phillips has been essential through her understanding of the unique meteorological possibilities provided by NMC and her acceptance of the special efforts that are sometimes necessary to exploit those possibilities.

TABLE OF CONTENTS

LIST OF TABLES

LIST OF ILLUSTRATIONS

THE NESTED GRID MODEL

Norman A. Phillips
National Weather Service, National Meteorological Center, NOAA,
Camp Springs, Md.

ABSTRACT. The nested grid model (NGM) consists of a stereographic hemispheric grid with the option of one or two interior rectangular grids, each of successively smaller area and finer horizontal resolution. The location and number of the vertical sigma levels is flexible, as is the basic horizontal resolution. Second-order accurate finite-difference formulas are used, in a two-step Lax-Wendroff procedure. Special initial treatments are used to reduce spurious gravity waves from the Himalayas, and to insure symmetry about the Equator.

Details of the September 1978 state of the model and its numerical procedures are presented, including the representation of latent heat release, small-scale vertical exchange, spatial filtering, grid meshing at boundaries, and data input from the Flattery global analysis system at NMC. (Radiation is not yet included in the NGM.) A brief review of experimental results is presented.

CHAPTER I: BASIC CONCEPTS

The nested grid model (NGM) was constructed beginning in late 1974 to serve as a research model at NMC and as a possible candidate for operational implementation. Flexibility of its structure was therefore important.[1]

In the vertical direction, a simple "sigma" coordinate is used:

$$\sigma = 1 - p/H \tag{1.1}$$

where p is pressure,[2] and

$$H = \text{surface pressure.} \tag{1.2}$$

---

[1]This was facilitated by the availability of the PL1 preprocessor which allows array dimensions in Fortran statements to be changed at will.

[2]Pressure in the NGM code and data is expressed in units of 100 cb (= 1 bar). Otherwise, units are in meters, seconds, and tons.

(Note that opposite to usual usage, σ increases from 0 at the ground to 1 at the top of the atmosphere.) The vertical discretization was patterned after that suggested by Arakawa (Arakawa and Mintz 1974), and is illustrated in figure 1.1. (For notational convenience, we follow Arakawa and use a caret to denote variables located at an interface, while the same symbol without the caret denotes a quantity in the layer located above the interface with the same subscript k.) The distribution and number of sigma layer thicknesses $\Delta\sigma_k$

$$\begin{aligned} &\Delta\sigma_k = \hat{\sigma}_{k+1} - \hat{\sigma}_k, \quad (k = 1,\ldots,K) \\ &\sum_{k=1}^{K} \Delta\sigma_k = 1, \end{aligned} \tag{1.3}$$

was left open and is set by input data cards in the initial data code associated with this model. The model therefore does not contain either a unique thin boundary layer next to the ground, nor a "tropopause," such as exists in current operational NMC models.

Various choices of $\Delta\sigma$ have been used, all of which, like the pattern used at the Geophysical Fluid Dynamics Laboratory (Miyakoda 1973), have smaller values of $\Delta\sigma$ at the top and bottom of the atmosphere, with larger values in between. In a 10-level version (K = 10), for example, the values were chosen symmetrically as follows:

k = 1 and 10	0.070
k = 2 and 9	0.078
k = 3 and 8	0.090
k = 4 and 7	0.109
k = 5 and 6	0.153

(1.4)

Meaningful tests of the effect of varying these sigma increments have not yet been made.

The nested aspect of the NGM is illustrated in figure 1.2. This figure is a stereographic map, and the finite-difference formulation of the forecast equations is done in stereographic coordinates x,y:

$$(x, y) = 2a \frac{\cos\Theta}{1 + \sin\Theta} (\cos\lambda, \sin\lambda) \tag{1.5}$$

where a, Θ, and λ are the radius of the Earth, geographic latitude, and longitude.

The outer grid, denoted by A, is a square array in which i and j each run in the x and y directions from 1 through 2·NH+6. The North Pole on this grid is located at

$$i = j = NH+4. \tag{1.6}$$

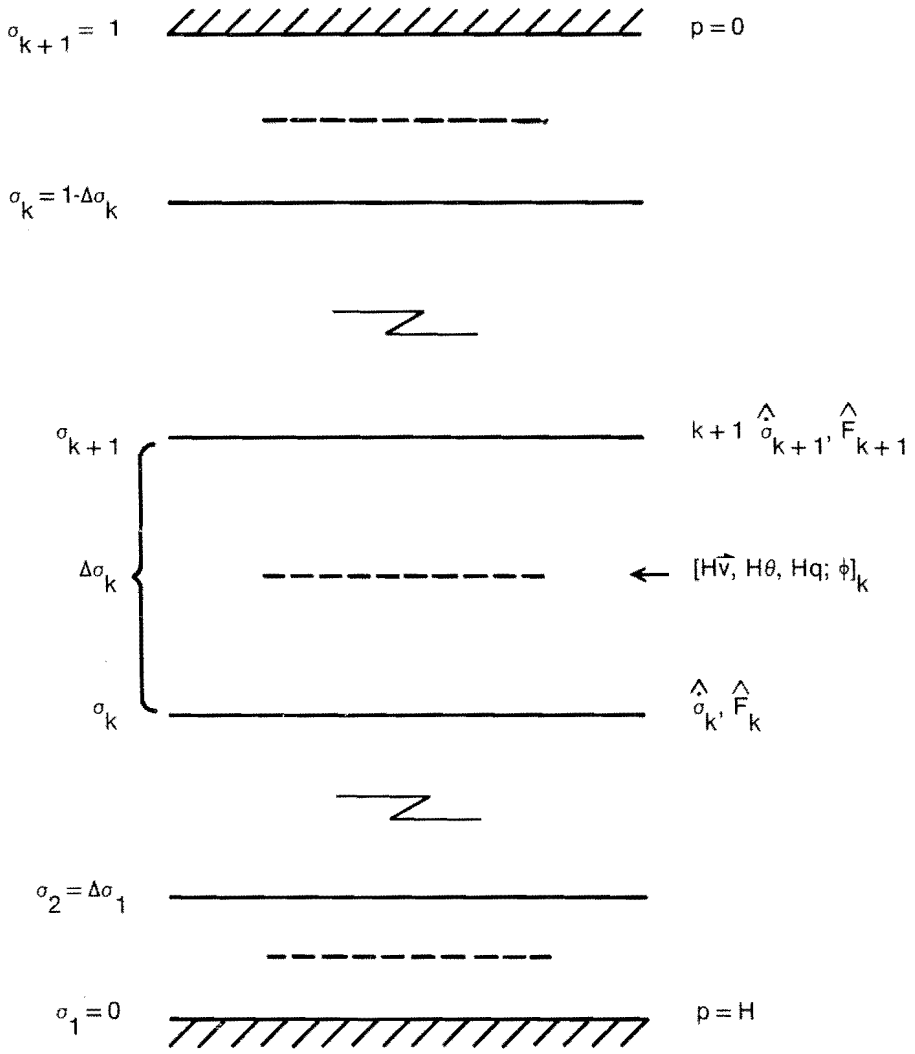

Figure 1.1.--Vertical structure of the NGM showing the location of interfaces (solid lines) and layers (dashed lines), and the variables defined at those positions.

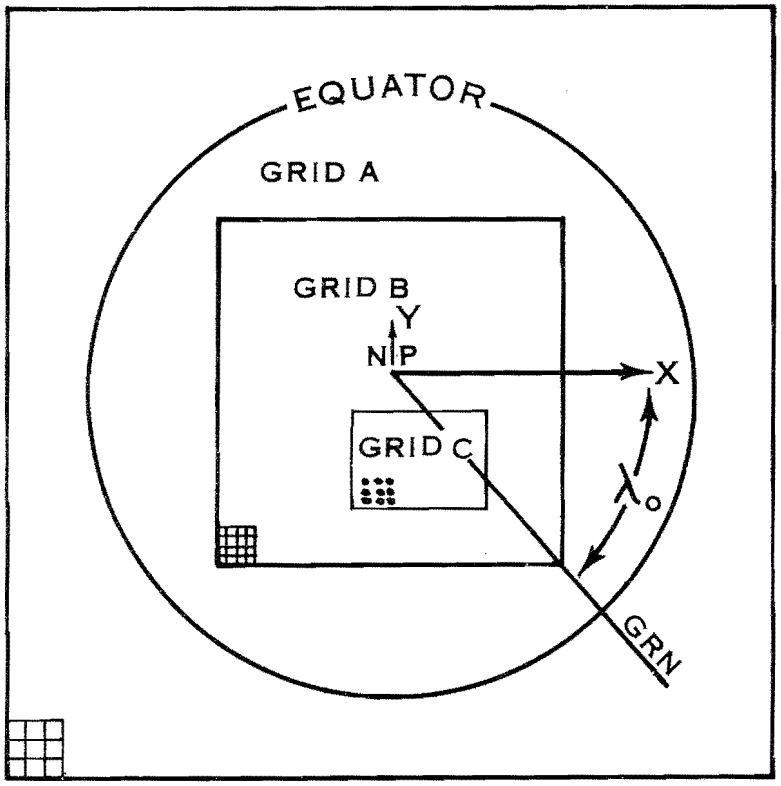

Figure 1.2--Three-grid structure of the NGM, and its orientation with respect to the Greenwich meridian (GRN).

The integer NH determines the horizontal grid spacing Δ on this grid:

$$\Delta_A = \frac{2a}{NH+0.5}. \tag{1.7}$$

The outer boundaries of grid A therefore extend at least 2.5 grid increments into the Southern Hemisphere. This extension is to facilitate applying a lateral boundary condition at the Equator (see Appendix I).

Grid A is used in every forecast, but located within it is an optional grid B, having twice the resolution of grid A:

$$\Delta_B = \tfrac{1}{2}\Delta_A. \tag{1.8}$$

A third grid, C, can also be located within grid B, with still finer resolution:

$$\Delta_C = \tfrac{1}{2}\Delta_B = \tfrac{1}{4}\Delta_A. \tag{1.9}$$

The model can therefore be run in three formats: only grid A; grids A and B; or grids A, B, and C.

The grid lines of grids B and C are parallel to those of grid A, but both interior grids may have differing x and y dimensions given by the ranges i = 1,...,IM, and j = 1,...,JM, so that their areas can be rectangular in shape.

The final horizontal degree of freedom is that the positive x-axis of grid A, defined by eq (1.5) as the line $\lambda = 0$, may be rotated an arbitrary amount λ_o eastward from Greenwich:

$$\lambda = \tan^{-1}\left(\frac{y}{x}\right) = \lambda_G - \lambda_o, \tag{1.10}$$

where λ_G is longitude measured eastward from Greenwich.[1]

The time step Δt for each grid is proportional to its grid increment, so that the ratio

$$\varepsilon = \Delta t/\Delta \tag{1.11}$$

is the same for all three grids. The time stepping procedure is illustrated in figure 1.3 for the most general case of three grids. A complete time-step cycle in this three-grid format consists of seven forecast steps. First there are two time steps on grid C, followed by a single time step on grid B (steps 1, 2, 3). This is followed by an interpolation process, denoted by an asterisk, during which the outer boundary points of grid C are updated by an interpolation from grid B, and those interior points on grid B in the vicinity of the edges of C are updated by interpolation from grid C.[2] Following this interpolation, the forecasting is resumed on grids C and B in steps 4, 5, and 6. After they have again been mutually interpolated, grid A is forecast for one time step in step 7. This is followed by an interpolation between grids B and A similar to that between B and C. The final process is to update the outer subequatorial points of grid A by applying the equatorial symmetry condition of

$$a\ d\ \theta/dt = 0 \tag{1.12}$$

$$\frac{\partial}{\partial\theta}\left(a\cos\theta\frac{d\lambda}{dt}\right) = \frac{\partial\theta}{\partial\theta} = \frac{\partial H}{\partial\theta} = 0 \quad (\theta \text{ is potential temperature}).$$

---

[1]The choices $\lambda_o = 10^o$ and -15^o result in the negative y-axis of figure 1.2 being located at 80°W and 105°W, corresponding to the orientation of the PE and LFM grids used at NMC

[2]The grids overlap just enough for this interpolation process to be carried out, as described in Appendix H.

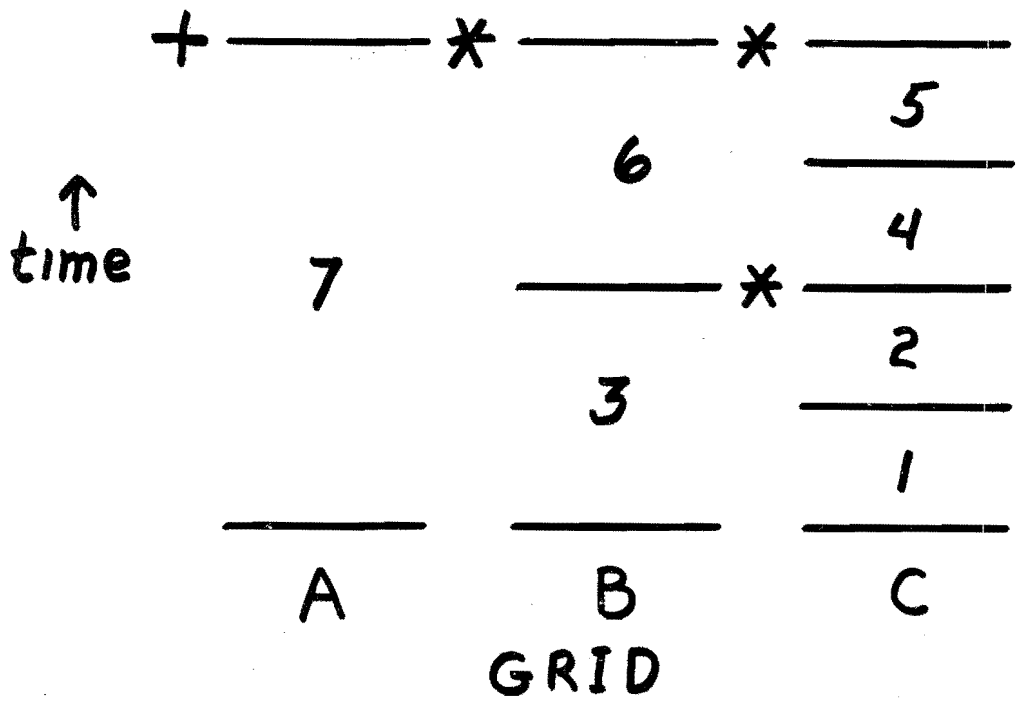

Figure 1.3.--Time stepping required for grids C, B, and A. Mutual boundary interpolations are denoted by an asterisk. The final equatorial treatment on grid A is indicated by the plus sign.

This nesting procedure is a "two-way" interaction in the terminology of Phillips and Shukla (1973). It has the virtue that gravity waves on an interior grid can disperse freely outward across its boundaries. The reduction in grid size by a factor of only two between neighboring grids minimizes possible differences in computational phase speeds, and any peculiar boundary reflections and trapping to which this difference might give rise. At the same time, the structure shown in figure 1.3 insures that if it is the forecast on grid C which is of major interest, most (~4/7) of the computational work will in fact be spent on that grid.

As a practical matter, it may be mentioned that the hemispheric output codes developed for this model obtain a desired output gridpoint value on an arbitrary hemispheric stereographic output grid by simple interpolation only on the finest of the three forecast grids that has a forecast grid square containing the desired output gridpoint. No trace of the underlying forecast grid boundaries has ever showed up on output maps constructed in this way.

A typical computing requirement for the NGM is 36 min of CPU time on an IBM 360/195 for a 24-hr forecast using a 10-level version with two grids; grid A having NH=27, and grid B having 51 x 59 gridpoints. Under favorable system conditions, this must be supplemented by only 10-15 percent input-output time for core-disk transfers. The required core storage is approximately IMMx295x(K+1) words, where IMM is the maximum i length of a grid row (normally IMM=2NH+6). The configuration defined above requires about 195000 words of core storage. (Single precision floating point numbers are used: in the IBM 360/195 system one such word or number = 4 bytes = 32 binary places, with a precision of about 7 decimal digits.)

CHAPTER II: GRID STRUCTURE AND FORECAST EQUATIONS

The basic forecast variables in the NGM are

H = surface pressure

Hθ = sfc. pressure x potential temperature

Hu = sfc. pressure x x-velocity component

Hv = sfc. pressure x y-velocity component

Hq = sfc. pressure x specific humidity

The last four variables are all located within the sigma layers of figure 1.1. Some two-dimensional surface fields are also carried.

ϕ_g = ground geopotential

PRCP = accumulated forecast precipitation

ST = ground (or water) temperature

SR = surface roughness

SM = ground or water moisture

SA = surface albedo

SS = snow cover

In the present form of the NGM, radiation is not included in the "physics," so that turbulent heat flux from land cannot be computed. ST is therefore irrelevant over land at this time, as are SM, SA, and SS.

The forecast procedure on any one of these grids to do one time step, Δt_A or Δt_B or Δt_C (i.e., <u>one</u> of the seven forecast operations on figure 1.3), is a "two-step" second-order Lax-Wendroff process (Phillips 1962; Lax and Wendroff 1964). It uses the Eliassen time and horizontal staggering of variables (Eliassen 1956). At the beginning (and end) of the double steps, the variables are located horizontally as shown in figure 2.1. At the intermediate half-time step, forecast values of H, θ, and q are computed in the center of the grid square (denoted by H′, θ′, and q′) while forecast values of u and v (denoted by u′ and v′) are computed in the locations of Hv and Hu. These primed variables are valid at $t + \frac{1}{2}\Delta t$. They are then used to compute the derivatives needed in taking the original variables a full time step from t to $t + \Delta t$. (The two-dimensional fields ϕ_g,...,SS are located at the H points of figure 2.1. They have no half time-step counterpart.)

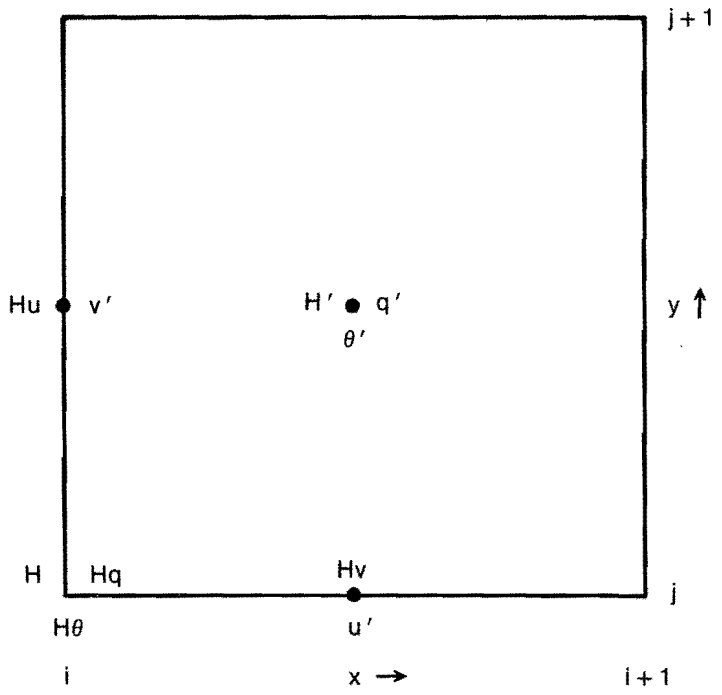

Figure 2.1.--Location in a grid square of the full time-step variables H, Hu, Hv, Hθ, Hq, and the half time-step variables H′, u′, v′, θ′, and q′.

Advantages of this Lax-Wendroff procedure with the Eliassen grid are as follows:

a. It has no computational modes and is slightly damped. This feature seems to result in better meshing between adjacent grids (Phillips 1962; Phillips and Shukla 1973).

b. In the computations, core limitations require that successive j-strips of data be read in and out of core. Only one strip need be read in for every forecast strip read out, whereas a leap-frog procedure requires two old strips to be read in for each new forecast strip.

c. The time-averaging procedures (or occasional uncentered restarts) that are often necessary in leap-frog techniques are not needed.

d. The small local horizontal averaging involved (which gives rise to the small damping) eliminates the $\sqrt{2}$ factor multiplying the magnitude of the horizontal wind in the computational stability criterion (see Chapter VIII.)

e. Gravity wave propagation is treated more accurately than in the Shuman procedure generally used at NMC (Shuman and Hovermale 1968; Gerrity 1977).

The disadvantages are

f. Separate codes are necessary for the half and full time-step.

g. About twice as much arithmetic is required per double Lax-Wendroff time-step as is needed in the Shuman procedure for a single leap-frog step.

Disadvantage f is a minor problem, but disadvantage g is potentially serious. A careful design of the computation strategy, core storage, and detailed "do-loop" structure to reduce CPU time was therefore planned from the beginning. Some success in attaining efficiency is shown by comparative CPU times. The NGM takes 1.46×10^{-4} sec per grid point per level for the Lax-Wendroff double time step, compared to the 1.05×10^{-4} sec per grid point per level required by the current operational seven-level hemispheric model for each leap-frog time step.

Both the half time step and full time steps use the hydrostatic equation

$$\partial\phi/\partial\pi = - c_p\theta, \tag{2.1}$$

in which

$$\phi = \text{geopotential} = gz$$

$$\pi = p^{R/c_p} \tag{2.2}$$

$$\theta = \text{potential temperature},$$

to compute the geopotential from forecast values of H (surface pressure), θ, and the known ground geopotential

$$\phi_g = g \times \text{ground height.} \tag{2.3}$$

Both time steps also use the continuity equation in sigma coordinates:

$$\frac{\partial H}{\partial t} = - H \frac{\partial \dot{\sigma}}{\partial \sigma} - \text{div}(H \vec{v}). \tag{2.4}$$

The horizontal velocity $\vec{v}$ has x and y components u,v;

$$u = \frac{1}{m}\frac{dx}{dt} = - \cos\lambda\left(a \frac{d\theta}{dt}\right) - \sin\lambda\left(a \cos\theta \frac{d\lambda}{dt}\right), \tag{2.5}$$

$$v = \frac{1}{m}\frac{dy}{dt} = - \sin\lambda\left(a \frac{d\theta}{dt}\right) + \cos\lambda\left(a \cos\theta \frac{d\lambda}{dt}\right), \tag{2.6}$$

The map scale factor is

$$m = \frac{2}{1 + \sin\theta} = 1 + \frac{x^2 + y^2}{4a^2}. \tag{2.7}$$

The divergence operation in stereographic coordinates is

$$\text{div}(H \vec{v}) = m^2 \left(\frac{\partial}{\partial x}\left(\frac{Hu}{m}\right) + \frac{\partial}{\partial y}\left(\frac{Hv}{m}\right)\right). \tag{2.8}$$

The boundary conditions $\dot{\sigma} = 0$ at $\sigma = 0$ and 1, when applied to the vertical integral of eq (2.4), yield the surface pressure tendency equation:

$$\frac{\partial H}{\partial t} = - \int_0^1 \text{div}(H \vec{v}) d\sigma. \tag{2.9}$$

This is used in both time steps to predict H and H′, and, after substitution in eq (2.4), to enable $\dot{\sigma}$ to be computed from

$$\frac{\partial(\dot{\sigma}H)}{\partial \sigma} = - \left(\frac{\partial H}{\partial t} + \text{div}(H \vec{v})\right).$$

The form of the remaining basic forecast equations differs in the two time steps, however.

In the half time step, the "advective" form is used. Let us define the advective operator A on an arbitrary scalar h by

$$\frac{dh}{dt} = \frac{\partial h}{\partial x} + \vec{v}\cdot\nabla h + \dot{\sigma}\frac{\partial h}{\partial \sigma}$$

$$= \frac{\partial h}{\partial t} + m\left(u\frac{\partial h}{\partial x} + v\frac{\partial h}{\partial y}\right) + \dot{\sigma}\frac{\partial h}{\partial \sigma} \qquad (2.11)$$

$$= \frac{\partial h}{\partial t} + A\,h.$$

The half time step equations then use the following prediction equations for u, v, θ, and q.

$$\frac{\partial u}{\partial t} = -\,Au - m\left(\frac{\partial \phi}{\partial x} + c_p\,\theta\frac{\partial \pi}{\partial x}\right) + f'v + F_x, \qquad (2.12)$$

$$\frac{\partial v}{\partial t} = -\,Av - m\left(\frac{\partial \phi}{\partial y} + c_p\,\theta\frac{\partial \pi}{\partial y}\right) - f'u + F_y, \qquad (2.13)$$

$$\frac{\partial \theta}{\partial t} = -\,A\theta + \frac{1}{\pi c_p}\left(Q_{turb} + Q_{rad}\right) \qquad (2.14)$$

$$\frac{\partial q}{\partial t} = -\,Aq + \dot{q}_{turb}. \qquad (2.15)$$

In these equations, f′ is a modified Coriolis parameter (Ω = 7.29 x 10^{-5}/sec = angular rotation of the Earth)

$$f' = 2\Omega\sin\Theta + (uy - vx)/2a^2 \qquad (2.16)$$

F_x, F_y, Q_{turb}, and $\dot{q}_{turb}$ are the horizontal frictional forces, heating, and moisture changes arising from small-scale vertical turbulent exchange. They are described in Chapter III. (The NGM has no explicit horizontal diffusion except for the special purpose filtering described in Chapter V.) Q_{rad}, the heating from radiation, has not yet been introduced in the NGM, and is written symbolically in eq (2.14) only for completeness at this time. Note that eq (2.14) and (2.15) do not contain contributions from condensation of water vapor. This is included only at the end of the full time step, which is now described.

The full time step equivalent of eq (2.12)-(2.15) is written in "flux" form, based on the following relation for an arbitrary scalar h:

$$\frac{\partial(Hh)}{\partial t} = H\,\frac{\partial h}{\partial t} + h\,\frac{\partial H}{\partial t}$$

$$= H\left(-\,Ah + \frac{dh}{dt}\right) - h\left(H\,\frac{\partial \dot{\sigma}}{\partial \sigma} + \mathrm{div}(H\vec{v})\right)$$

$$= -\left(\frac{\partial}{\partial \sigma}(\dot{\sigma}\,Hh) + \mathrm{div}(\vec{v}\,Hh)\right) + H\,\frac{dh}{dt}$$

$$= -\,B(Hh) + H\,\frac{dh}{dt}\,.$$

Using the flux operator B so defined, the equations for the full time step are

$$\frac{\partial Hu}{\partial t} = -\,B(Hu) - m\left(\frac{\partial H\phi}{\partial x} - (\phi - R\pi\theta)\frac{\partial H}{\partial x}\right) + H(f'v + F_x), \tag{2.17}$$

$$\frac{\partial Hv}{\partial t} = -\,B(Hv) - m\left(\frac{\partial H\phi}{\partial y} - (\phi - R\pi\theta)\frac{\partial H}{\partial y}\right) + H(-\,f'u + F_y) \tag{2.18}$$

$$\frac{\partial H\theta}{\partial t} = -\,B(H\theta) + \frac{H}{\pi c_p}\left(Q_{turb} + Q_{rad} + Q_{cond}\right), \tag{2.19}$$

$$\frac{\partial Hq}{\partial t} = -\,B(Hq) + H\left(\dot{q}_{turb} + \dot{q}_{cond}\right). \tag{2.20}$$

The pressure force terms in eq (2.17) and (2.18) are written in this manner instead of $H(\partial\phi/\partial x + c_p\theta\ \partial\pi/\partial x)$, to provide exact momentum conservation properties. (See Appendix B.) The latent heat terms Q_{cond} and $\dot{q}_{cond}$ are now evaluated by means of the adjustment process described in Chapter IV.

To summarize: In the half time step, eq (2.1), (2.9), (2.10), and eq (2.12)-(2.15) are used to compute (H', θ', q', u', and v') at time $t + 0.5\ \Delta t$ as located in figure 2.1 from the values of H. $H\theta$, Hq, Hu, and Hv at time t in that figure. Then eq (2.1), (2.9), (2.10), and (2.17)-(2.20) are used to compute (H, $H\theta$, Hq, Hu, and Hv) at time $t + \Delta t$ at their original locations. In this last process the primed variables at $t + 0.5\ \Delta t$ are used in evaluating the B term, the pressure gradient and Coriolis terms on the right side of eq (2.17)-(2.20), and the complete right sides of eq (2.1), (2.9), and (2.10).

CHAPTER III. SURFACE FLUXES AND TURBULENT VERTICAL TRANSPORTS

The frictional terms F_x, F_y in the horizontal equations of motion and the turbulence contributions Q_{turb} and $\dot{q}_{turb}$ can all be written in the general form $\partial Fh/\partial\sigma$, where Fh represents the turbulent downward flux of the property h through a sigma surface. At the surface ($\sigma = 0$) these fluxes take the conventional form

$$\begin{aligned} FU &= F_1 \cdot u_{air} \\ FV &= F_1 \cdot v_{air} \\ FT &= F_1 \cdot (T_{air} - T_{surface}) \\ FQ &= F_1 \cdot (q_{air} - q_{surface}) \end{aligned} \tag{3.1}$$

where F_1 is an aerodynamic coefficient (modified to allow for $\rho dz = dp/g = H\, d\sigma/g$):

$$F_1 = g \left(\frac{\rho}{H}\right) C_D |\vec{v}|_{an} \tag{3.2}$$

(ρ is density.) For bottom layers of thickness 5-10 cb, it has proved worthwhile to set $|\vec{v}|_{an}$ at a fraction "ANEM" = 0.8 of the wind speed in layer k=1 of the model. ρ/H is approximated by the inverse of the constant RT = (287.05)(273).

The drag coefficient C_D consists of two factors:

$$C_D = C_{Dv} \cdot C_{Dr}$$

where C_{Dv} represents a simple empirical dependence on $|\vec{v}|_{an}$:

$$C_{Dv} = (0.7 + 0.07\ |\vec{v}_{an}|)/1.296. \tag{3.3}$$

C_{Dr} is the measure of surface roughness derived by Cressman (1960), having the value of 1.296×10^{-3} over oceans and reaching a maximum value of 8.5×10^{-3} over the central Rockies and Tibet. This results in a value of $C_D = (0.7 + 0.07|\vec{v}_{an}|) \times 10^{-3}$ over oceans, as used by Ooyama (1969).

The surface fluxes FT and FQ in eq (3.1) are only computed over oceans, using $T_{air} = H^{R/c_p}$ times θ from layer 1 and $q_{air} = q$(layer 1). Over land, FT and FQ are at this time set equal to zero, since $T_{surface}$ over land cannot be predicted without a heat balance condition for the soil, which in turn requires knowledge of the missing radiation fluxes. Over water, $T_{surface}$ is the same sea-surface temperature field used by regular NMC models, and $q_{surface}$ is the corresponding saturation specific humidity.

u_{air} and v_{air} in eq (3.1) are reduced by the same factor ANEM from the u and v of layer 1 to anemometer level, and also rotated by an angle of 22.5^{o}, counterclockwise in the Northern Hemisphere, clockwise in the Southern Hemisphere.

In the interior, at interfaces $\hat{\sigma}_k$, k = 2,...,K, the sigma form for the flux Fh, derived from the conventional austausch form, is

$$Fh = \frac{\rho^2 g^2}{H^2} A \frac{\partial h}{\partial \sigma} \tag{3.4}$$

where A, of dimension m^2/s, is a kinematic austausch coefficient. Fh is evaluated by first simplifying $\rho\, g/H = (1 - \hat{\sigma}_k)(g/RT)$ to $(1 - \hat{\sigma}_k) \div (7440\ m)$ and then defining the exchange coefficient $\hat{F}_k$:

$$\hat{F}_k(k = 2,...,K+1) = \left(\frac{1-\hat{\sigma}_k}{7440}\right)^2 \frac{2}{(\Delta\sigma + \Delta\sigma_{k-1})} \hat{A}_k \tag{3.5}$$

where $\hat{A}_k$ is prescribed as a simple function of the Richardson number, Ri:

$$\hat{A}_k = \frac{A_{lim}}{\frac{1}{4} + |\hat{Ri}|_k} . \tag{3.6}$$

Then, for h = u, v, θ, or q, we have a general formula for the interface flux at k = 2,...,K+1:

$$(\hat{Fh})_k = F_k^{\bullet} (h_k - h_{k-1}) \tag{3.7}$$

At the top of the atmosphere (k = K+1), $\hat{\sigma}_k = 1$, so $\hat{F}_k$ vanishes there.

No remarkable virtues are associated with the crude expression eq (3.6) for A except that it does increase the vertical exchange with smaller Ri. A_{lim} has normally been set at 50 m^2/s. For typical free atmosphere Ri values of 30, A is then about 2 m^2/s. This produces a negligible effect on the large-scale interior motion:

$$F_x \sim A\frac{\partial^2 u}{\partial z^2} \sim 2\frac{(25)}{(7000)^2} \sim 10^{-6}\ m \cdot s^{-2} . \tag{3.8}$$

This is only about 0.1 percent of the typical Coriolis acceleration. For the exceptional case of Ri $\sim$ 0, A is about 200 m^2/s. Here the danger is violation of the CFL criterion for vertical diffusion, which is (approximately),

$$A < \frac{(\Delta z)^2}{4\Delta t} , \tag{3.9}$$

where Δz is the height increment corresponding to $\Delta\sigma$. The 700-m value of Δz implied by the $\Delta\sigma$ = 0.07 of (1.4), together with a typical time

step of 1/7 hr on grid A requires $A \leq 238\ m^2/s$. This computational stability criterion was used in fact to set A_{lim} at 50 m^2/s for $\Delta\sigma$'s of the type listed in eq (1.4). For smaller $\Delta\sigma$, either A_{lim} or Δt would have to be reduced. (In view of our ignorance about turbulent exchange, the prudent person would of course reduce A_{lim}.)

At the present time, the meteorological effect of this somewhat arbitrary vertical turbulence flux in the free atmosphere is minor. It has produced some beneficial stabilizing tendency in extremely strong baroclinic jets (90 m/s) that occur in winter. It does produce an average downward heat flux equivalent to a net warming of several tenths of a degree per day in the lower troposphere and thereby contributes to a slight warm bias in predicted temperatures. The eventual introduction of radiation into the NGM (and a surface heat balance condition over land) should act to correct this.

A dry adiabatic adjustment is incorporated into the prediction of $H\theta$. Immediately after new values of $H\theta$ have been computed in the full time step of the Lax-Wendroff procedure (but before saturation is considered), the vertical distribution of θ is examined at each grid point column for instances of $\theta_{k+1} < \theta_k$. If adjacent layers $k = k_1$, to $k = k_2$ have decreasing values of θ, they are all adjusted to the same value of θ,

$$\theta_{adj} = \sum_{k_1}^{k_2} \pi_k \theta_k \Delta\sigma_k \div \sum_{k_1}^{k_2} \pi_k \Delta\sigma_k . \qquad (3.10)$$

This adjustment preserves the (dry) enthalpy of the column. It produces a slight increase in the mean θ, but this is to be expected since the adjustment process envisages an unstable potential density distribution breaking up into turbulent motion, which is then converted to heat by viscosity (Rossby 1932). The process is repeated until no layer has θ greater than the layer below.[1]

This adjustment can change θ by 1 to 2 degrees in the initial data obtained from the global Flattery isobaric height analyses (see Chapter VI). However, adjustments of as much as 0.5 degree never occur in a forecast.

---

[1]Efficient programming of this examination is patterned after a routine developed by J. Stackpole.

CHAPTER IV. LATENT HEAT RELEASE AND MOIST CONVECTION

This consists of two successive adjustment processes in the NGM:

a. A modified Kuo simulation of organized cumulus and cumulo-nimbus convection.

b. Large-scale saturation adjustment.

They are applied only at the end of the Lax-Wendroff two-step process; they are not used at the half time step.

The convection process is patterned after Kuo's original scheme (Kuo 1965). It is not to be thought of as modeling isolated thunderstorms, such as occur from afternoon heating, but rather as modeling the organized moist convective process brought about by the simultaneous occurrence of three factors: large-scale convergence of moisture, a moist unstable lapse rate, and at least moderately high relative humidity. As such, it can be viewed as a slightly more sophisticated version of the moist-adiabatic lapse-rate adjustment used at the Geophysical Fluid Dynamics Laboratory (Miyakoda 1973).

Because the Kuo computation can be time consuming, the NGM uses a preliminary screening test patterned after one successfully used by Hovermale. Let DHQ_k represent the change in Hq for layer k predicted in the current (full) time step by all processes except condensation [(i.e., except $\dot{q}_{cond}$ in eq (2.20)]. The possibility of the Kuo process is ignored in the NGM unless

$$\sum_{k=1}^{KACUM} DHQ_k \cdot \Delta\sigma_k > \Delta t \cdot 5 \times 10^{-6} \text{ cb/s.} \qquad (4.1)$$

(KACUM is usually set at 4.) A horizontal convergence rate of -10^{-5}/s will produce large enough DHQ to satisfy this if the specific humidity is of order 10^{-2}.

If the test eq (4.1) is satisfied, the second test is to take a parcel from layer 1, with its provisionally forecast pressure and temperature, assume it is saturated, and determine to how high a layer it can be lifted moist adiabatically before it becomes colder than the temperature in that layer. As soon as two successive layers k_2 and k_3 are found to be warmer than the lifted parcel, the unstable region is defined as extending from k = 1 through k = KTOP = k_2 - 1.[1]

---

[1]The requirement for two successive stable layers simplifies the decision process where the lapse rate is moist adiabatic except for small irregular deviations.

Having located a column of large enough water accumulation and an unstable moist stratification, the following sums over the layers k = 2 through KTOP are computed:

$$\text{WATER} = \frac{1}{g} \sum \text{DHQ}_k \cdot \Delta\sigma_k, \tag{4.2}$$

$$\text{Q1} = \frac{H}{g} \sum (q_{cld} - q_k) \cdot \Delta\sigma_k, \tag{4.3}$$

$$\text{Q2} = \frac{c_p H}{Lg} \sum (T_{cld} - T_k) \cdot \Delta\sigma_k, \tag{4.4}$$

$$\text{QEFF} = \text{WATER}/(\text{Q1} + \text{Q2}), \tag{4.5}$$

where q_{cld} and T_{cld} are the lifted parcel values of saturation humidity and temperature at layer k, L = 2.5 x 10^6 kJ/ton is the latent heat, and the sums in eq (4.3) and (4.4) only include layers for which $q_{cld} - q_k > 0$ or $T_{cld} - T_k > 0$, respectively. Q1 is the amount of water needed to fill the unstable layers with clouds, and Q2 is the amount of water vapor whose enthalpy would be enough to increase the dry enthalpy of the existing lapse rate to that of the cloud.

The Kuo changes in T and q for layers k = 2,...,KTOP are then given by

$$\text{DTKUO}_k = \text{QEFF} \cdot (T_{cld} - T_k), \tag{4.6}$$

$$\text{DQKUO}_k = \text{QEFF} \cdot (q_{cld} - q_k), \tag{4.7}$$

except that negative values are replaced by zero. The sum over k of eq (4.6) times $c_p \cdot \Delta\sigma_k$ plus eq (4.7) times $L \cdot \Delta\sigma_k$ is equal to the sum

$$L \sum \text{DHQ}_k \cdot \Delta\sigma_k.$$

DTKUO represents a temperature increase due to convective precipitation, and is to be added to the already forecast values of $H\theta_k$ at the new time step, but DQKUO (when multiplied by H), represents a revised version of DHQ. As such it is added to the Hq from the previous time step in place of adding the original DHQ.

A weakness of the scheme described above is that it will predict some convective precipitation even when the environment is dry enough that entrainment would quickly evaporate convective clouds as they extend into the drier regions above. (In other words, under these dry (but unstable) conditions in nature, all of QEFF goes into DQKUO even if $T_{cld} > T$.) To correct this, the NGM contains a simple modification. The condensate

$$(c_p/L)\text{DTKUO}_k \cdot \Delta\sigma_k \tag{4.8}$$

produced in layer k (k = 2,...,KTOP) is allowed to fall, subject to

the condition that it must evaporate until each layer through which it falls has reached a relative humidity of (arbitrarily) 90 percent of the relative humidity criterion used in the large-scale saturation process described below. The obvious cooling adjustment in DTKUO is made for each layer experiencing such evaporation. This modification seems to have eliminated the falsely computed convective zones in question.

The purpose of this moist convection adjustment process is to prevent calculations being made with the nonturbulent equations alone under conditions of static instability (where they are inadequate). The process as described above seems to have performed this function well in all computations so far with the NGM, except for one case described in NMC Office Note 171 (Phillips 1978). In that example, readily identifiable (and deleterious) consequences of explicit large-scale release of moist instability were experienced:

a. when the initial moisture distribution in the warm air was clearly analyzed as too wet below 850 mb compared to radiosonde observations;

b. with a corrected humidity analysis, when the horizontal resolution was reduced from 99 to 62 km on grid C.

The first of these need not be a fault of the NGM, but the second strongly suggests that the moist convection process used in the NGM is not a satisfactory solution under all conditions.

The large-scale condensation process is an isobaric adjustment applied at every gridpoint, after the Kuo process has been applied at its selected columns. (The two top layers are not adjusted to saturation, since specific humidities at these heights are small.) The saturation adjustment is patterned after the isobaric constant enthalpy process, similar to the well-known 'wet-bulb' relation. Given a mixture of moist air at temperature T^o, total pressure p, and specific humidity q^o, such that q^o is greater than the saturation specific humidity at T^o, an (irreversible) isobaric constant enthalpy adjustment will produce saturation at temperature $T' > T^o$. After neglecting several small terms in q^o, this balance can be stated as

$$c_p(T' - T^o) = L[q^o - q_s(T')]. \tag{4.9}$$

Using the approximate relation

$$\left(\frac{\partial q_s}{\partial T}\right)_p = \frac{L}{R_v T^2} q_s = \alpha \cdot q_s, \tag{4.10}$$

q_s at the unknown temperature T' can be written

$$q_s(T') = q_s(T^o)[1 + \alpha \cdot (T' - T^o)]. \tag{4.11}$$

This can be evaluated after $T' - T^o$ is computed from eq (4.9) and (4.11):

$$T' - T^o = [q^o - q_s(T^o)]/[\frac{c_p}{L} + \alpha\, q_s(T^o)]. \qquad (4.12)$$

This approximate procedure succeeds in having the new adjusted q, given by eq (4.11), very close to the true saturation specific humidity at the new adjusted temperature T'. It avoids the undersaturation computed by using $q_s(T^o)$ instead of $q_s(T')$ for the adjusted q.

An important practical modification in the NGM to eq (4.11) and (4.12) is that large-scale saturation is defined as occurring at a fraction 0.9 of q_s. (Roughly similar saturation factors are used in NMC operational models.) A factor 0.9 is thereby introduced in front of the three $q_s(T^o)$ appearing in eq (4.11) and (4.12). Some experimentation was done with this factor. More testing should be done, but only with initial humidity analyses that are more reliable than provided by the current NMC analyses of water.

At the present time, all condensed water vapor falls immediately to the ground in this large-scale adjustment process; no allowance is yet made in the NGM for evaporation of falling drops and cloud storage.

An interesting example of forecast precipitation rates from the first precipitation forecast of the NGM is reproduced in figure 4.1. This is a time sequence of the forecast surface pressure, convective precipitation per time step and large-scale precipitation per time step at a fixed point in the Ohio valley during the passage of a spring storm. Only grid A was used, with a time step of 1/8 hr. Values are plotted at each time step. Of special note are

a. The smoothness of the two precipitation records.

b. The sudden termination of the convective precipitation at 17 hr [due to the test (4.1)] causes an immediate jump in the large-scale precipitation, so that the latter at the first time step without convective precipitation is almost as large as the total precipitation in the preceding time step.

c. The surface pressure changes very smoothly, but it is subject to appreciable oscillation with periods of 3-4 hr.

The large surface pressure oscillations shown here have been traced to external gravity waves, moving at speeds of about 300 m/s. They originate over the steep slopes of the Himalayas, Greenland, and the Rockies because of vertical truncation error in the evaluation of the horizontal pressure force,

$$\nabla_p \phi = \nabla_\sigma \phi + c_p \theta \nabla_\sigma \pi, \qquad (4.13)$$

in the presence of a sharp tropopause over steep orography. The

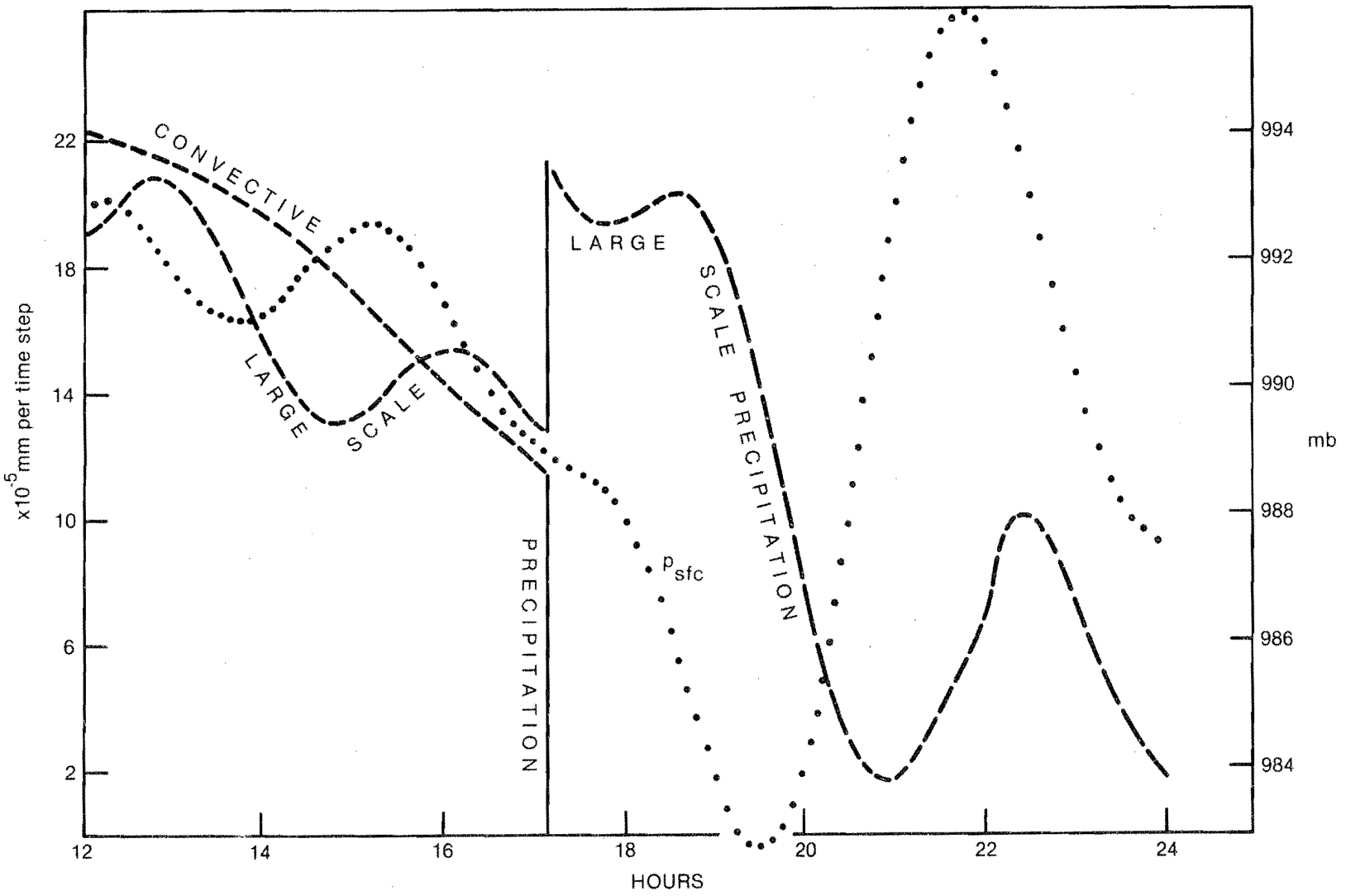

Figure 4.1.--12-24 hr record of surface pressure (one dot each time step) and precipitation rates, convective and large scale. (The dashes for the latter two are drawn connecting successive time step values.) Units are millibars and 10^{-5} mm per 7.5-min time step.

Himalayan slopes are by far the strongest source of these waves; Chapter VII describes the method now used in the NGM to reduce their effect.[1]

There is a pronounced correlation on figure 4.1 between rising surface pressure and minima in the large-scale precipitation rate, and falling surface pressure with maxima in the large-scale precipitation rate. The maximum pressure change in the wave is 1.3 cb between 19.5 and 21.75 hr. If this is experienced by a 50-cb thick saturated layer in which $(\partial q_s/\partial p)$ along a moist adiabat has the (observed) value 2×10^{-4}/cb, the precipitation in this period should be modified by an amount

$$1.3 \times \frac{50}{9.8} \times 2 \times 10^{-4} = 1.3 \times 10^{-3} \text{ (tons}\cdot\text{m}^{-2} = \text{m)}. \qquad (4.14)$$

When divided up between the 18 time steps in this 2¼-hr period, this yields a typical decrease in precipitation rate of 7×10^{-5} m/time step, reasonably close to the forecast dip in precipitation rate in this time interval shown on figure 4.1. As such it provides an interesting, albeit fortuitous test of the NGM large-scale precipitation mechanism.

Precipitation forecasts with the current (1978) NGM (almost none of which have been summer cases, however) appear to be at least as good as those made with the LFM and seven-layer operational models at NMC. An earlier version of the NGM suffered from severe short wavelength truncation error in the advection of specific humidity. This showed up as "wiggles" in the q values on a sigma surface in the generally dry air in back of a cold front. The wiggles had wavelengths in the range 2 to 4 grid increments and an amplitude large enough to produce negative values of q at their minima and slight supersaturation at their maxima. The resulting widespread areas of slight precipitation ($\leq$ 0.2 in./12 hr) seriously degraded the usefulness of the NGM precipitation forecasts (Stackpole 1978b).

Tests with fourth-order, accurate, three-dimensional advection of q did not correct this problem. The periodic filtering procedure described in Chapter V did ameliorate it to a considerable degree, however. Two examples of excellent 48-hr precipitation forecasts from the revised NGM are given in NMC Office Note 171 (Phillips 1978).

In common with other models, the NGM underpredicts precipitation in the first 9 hr. To some extent this may be because the initial velocity fields are nondivergent. The picture is complicated by uncertainties in the initial humidity analysis, however; some test forecasts with quasi-geostrophic deduced initial divergence fields on grid B of the

---

[1]The large ±6-mb oscillation in figure 4.1 centered around 20-22 hr is a wave that initially moves equatorward from the Himalayas, is reflected at the Equator, and then refocused over the United States. The initialization procedure described in Chapter VII typically reduces this wave to ±2 mb.

NGM have not shown a marked improvement in 0-12 hr precipitation amounts, even though these initial divergence fields seemed to be good. (It appears that the model will develop most of the correct divergence field in about 6 hr after a nondivergent start.)

Several obvious extensions of the present NGM precipitation scheme would be (a) extend the Kuo process so as to examine moist instability starting from higher layers (e.g., warm front thunderstorms), (b) experiment with the 90-percent saturation criterion, and (c) include evaporation of falling large-scale precipitation. It appears not worthwhile to do these, however, until better initial humidity analyses are available.

CHAPTER V: HORIZONTAL FILTERING

A smoothing operation [a low-order version of the type discussed by Shapiro (1975)] is applied every 3 hr to the forecast fields of u, v, θ, and q, on grids B and C. Let the operators L and M define the three-point second-difference operators on the grid point variable h_{ij} (h = u, v, θ, or q):

$$\begin{aligned} L\, h_{ij} &= (h_{i+ij} - 2h_{ij} + h_{i-ij})/4, \\ M\, h_{ij} &= (h_{ij+1} - 2h_{ij} + h_{ij-1})/4, \end{aligned} \tag{5.1}$$

and let the ranges of meaningful values of the unsmoothed variable h be

$$\begin{aligned} i &= IL \text{ to } IR \\ j &= JB \text{ to } JT. \end{aligned} \tag{5.2}$$

First, each i-row (for j = JB to JT) is treated as follows to give an i-smoothed value denoted by h'_{ij}.

Points i = IL and IR:

$$h'_{ij} = h_{ij}. \tag{5.3}$$

Points i = IL + 1 and IR - 1:

$$h'_{ij} = h_{ij} + L\, h_{ij}. \tag{5.4}$$

Points i = IL + 2 through IR - 2:

$$h'_{ij} = h_{ij} - L^2\, h_{ij}. \tag{5.5}$$

Following this, the final smoothed variable $\bar{h}_{ij}$ is obtained by the following operation on h'_{ij} (for i-columns i = IL through IR).

Points j = JB and JT:

$$\bar{h}_{ij} = h'_{ij}. \tag{5.6}$$

Points j = JB + 1 and JT - 1:

$$\bar{h}_{ij} = h'_{ij} + M\, h'_{ij}. \tag{5.7}$$

Points j = JB + 2 through JT - 2:

$$\bar{h}_{ij} = h'_{ij} - M^2\, h'_{ij}. \tag{5.8}$$

If the initial field is of the form

$$h_{ij} = \exp[\sqrt{-1}(\alpha i + \beta j)], \tag{5.9}$$

so that α and β define the x- and y-wavelengths,

$$\alpha = \frac{2\pi\Delta}{L_x}, \quad \beta = \frac{2\pi\Delta}{L_y}, \tag{5.10}$$

the response over the main interior region is

$$\overline{h}_{ij} = h_{ij} \times [1 - \sin^4 \frac{\beta}{2}][1 - \sin^4 \frac{\alpha}{2}]. \tag{5.11}$$

Two grid increment waves (for which $\alpha/2$ or $\beta/2$ is equal to $\pi/2$) are therefore completely eliminated. The individual factor $[1 - \sin^4 \alpha/2]$ takes the value 0.44 for a three grid-increment wave and 0.75 for a four grid-increment wave. It is greater than 0.95 for wavelengths greater than 6.4 grid increments.[1]

The basic variables Hu, Hv, Hθ, and Hq have the surface pressure H divided out before this smoothing operation and reinstated after the operation. H itself is not smoothed. In the first tests of this scheme, the complete variable array H, Hu, Hv, Hθ, Hq was smoothed directly. This proved satisfactory in regions and grids where the (fixed) surface orography ϕ_g had no energy in the 2-4 grid-increment scales, but introduced noticeable roughness in regions of more irregular ϕ_g when the horizontally smoothed data on sigma surfaces were interpolated onto constant-pressure surfaces. The roughness arose, of course, from the inconsistency of smoothing surface pressure but not orography in those regions. The variables u, v, and θ are filtered because the θ field occasionally develops the same type of irregularities as q to the rear of sharp cold fronts. This filtering of θ then suggested it was logical to filter u and v for dynamical consistency.

At the present time the forecast sigma fields are smoothed in this way only on grids B and C; the special programming necessary to smooth grid A with its roughly circular computational boundary has not been done.

---

[1]Some tests were made with the sharper operators L^3 and M^3 in eq (5.5) and (5.8) but the present ones seem adequate.

CHAPTER VI: INPUT DATA

The main source of initial atmospheric data for the NGM has been the global isobaric analyses of geopotential, wind, and relative humidity prepared by the "Hough" analysis program at NMC. In this program, developed initially by T. Flattery, simultaneous analyses of wind and geopotential are made. These two fields are constrained (separately for each zonal wavenumber and for each meridional wavenumber), by the kinematics of the Rossby-modes of the linearized theory of perturbations on a resting atmosphere.[1] From the practical aspect, a main consequence is horizontal velocity fields that have negligible divergence (an rms value $\sim 10^{-6}$/s) and that are in reasonably close geostrophic balance with the analyzed geopotential field. The analysis is truncated rhomboidally at wavenumber 24, which omits some small-scale features.[2] This is the analysis used for the operational Northern Hemisphere model at NMC.

Observations and some artificial "bogus" data are combined in the Flattery program with first-guess analyses provided by short-period forecasts from the nine-level global 2½ x 2½-degree latitude-longitude model (Stackpole 1978a).[3] The resulting global analyses are tabulated at intervals of 2.5 degrees in longitude and latitude on a "GLOPEP" data set, for the 12 standard surfaces 100, 85, 70, 50, 40, 30, 25, 20, 15, 10, 7, and 5 cb. Relative humidity analyses are also made for the lowest six surfaces 100-30 cb. The horizontal analysis program is carried out not for fields on individual pressure surfaces, but for the horizontal distribution of vertical empirical orthogonal functions, six functions being so analyzed for the wind and geopotential height fields, and three for the humidity fields. This vertical truncation from 12 to 6 and 6 to 3 results in some noticeable irregularities in derived temperature lapse rates in the high tropical troposphere and can produce unrealistic relative humidity profiles in the lower troposphere. The former of these activates most of the dry adiabatic adjustment at t = 0 referred to in Chapter III.

The field of surface geopotential ϕ_g used in the NGM was derived from the Northern Hemisphere heights at $1^{o}_{.}8 \times 1^{o}$ latitude-longitude points obtained some years ago by NMC from the Fleet Numerical Weather Center, supplemented by a 0.25 degree resolution orography set over the contiguous

---

[1]The relation used is only that for one vertical mode of the linear theory, corresponding to an "equivalent depth" of 11.5 km.

[2]For example, low-pressure centers over North America are often not analyzed deeply enough by as much as 60 m in geopotential.

[3]Ship air temperatures have been ignored, but are being introduced into the data base at the current time.

United States prepared by the Geophysical Fluid Dynamics Laboratory. This combined array on a 1^{o} x 1^{o} grid was then reflected into the Southern Hemisphere. The resulting global array was analyzed into a 72-wavenumber (triangular) spherical harmonic representation, and this truncated representation was then tabulated in the Northern Hemisphere onto a 1^{o} x 1^{o} latitude-longitude array. This array is now used to give surface heights (by interpolation) for the gridpoints of each NGM forecast grid by the input code.

This filtering of ϕ_g eliminates two-dimensional wavelengths in ground height shorter than 556 km, but as long as the horizontal space increment on grid A is smaller than this value there is compatibility in the orography seen by each of the three grids where they overlap. The smallness of 2 x 72 = 144 compared to 360 means that a "Gibbs phenomena" can be expected where high mountain ranges are close to the coast, as in the Gulf of Alaska and off the northwest coast of South America. The surface height reaches a minimum of around -200 and -75 m in these two oceanic regions. Over the rest of the oceans, the height field is characterized by ±10 m deviations from zero with typical wavelengths around 600 km. Strong smoothing of the narrow Cascades and Brooks ranges is the most noticeable meteorological weakness of this filtered orography field.

The input data for each NGM grid is obtained by horizontal and vertical interpolation from the Hough analysis. But before this is done, the global latitude-longitude data on the GLOPEP data set is subjected to a modification near the Equator. Let α be the following function of latitude:

$$\alpha(\theta) = 0.5 + \left(\frac{\theta}{20}\right) - \tfrac{1}{2}\left(\frac{\theta}{20}\right)^2, \qquad (6.1)$$

where θ is the Northern Hemisphere latitude in degrees. α varies monotonically from 0.5 at the Equator to 1 at $\theta = 20^{o}$, with a slope of zero at 20^{o}. The "even" variables E = zonal velocity, geopotential, and relative humidity, and the "odd" variable 0 = meridional velocity on the GLOPEP data set are then modified separately at each longitude by the following linear combination of Northern and Southern Hemisphere data:

$$\theta \geq 20^{o}: \quad \text{No change} \qquad (6.2)$$

$$0 \leq \theta < 20^{o}: \quad E'(\theta) = \alpha(\theta)\cdot E(\theta) + [1-\alpha(\theta)]\cdot E(-\theta), \qquad (6.3)$$

$$0'(\theta) = \alpha(\theta)\cdot 0(\theta) - [1-\alpha(\theta)]\cdot 0(-\theta). \qquad (6.4)$$

$$\theta < 0: \quad E'(\theta) = E'(-\theta), \qquad (6.5)$$

$$0'(\theta) = -\,0'(-\theta). \qquad (6.6)$$

This procedure produces even fields that smoothly approach the condition $\partial E/\partial\theta = 0$ at the Equator, and odd fields that smoothly approach zero at the Equator, in conformity with the boundary conditions eq (1.12). This will have some meteorological consequences, such as modifying the Intertropical Convergence Zone at 10^{o}N in the Pacific, and in eliminating all cross-equatorial flow. This seems a small price to pay, however, in a hemispheric model using nondivergent initial data.

The procedure does introduce divergence in low latitudes into the otherwise nondivergent initial winds. Since this divergence is meteorologically meaningless, the symmetrizing operations eq (6.2)-(6.6) are followed by an equatorial balancing program in the input code. Three operations are involved at each pressure surface:

a. The wind field between the Equator and 20^{o}N is made nondivergent:

$$\vec{v}_{new} = \vec{k} \times \nabla\psi \tag{6.7}$$

where the streamfunction ψ is determined from the vorticity of the just symmetrized wind

$$\nabla^2\psi = -\nabla\cdot\vec{k} \times \vec{v}_{sym}, \tag{6.8}$$

using the boundary conditions

$$\theta = 0: \quad \partial\psi/\partial\lambda = 0 \tag{6.9}$$

$$\theta = 20^{o}\text{N}: \quad \partial\psi/\partial\lambda = \left[a\cos\theta\left(a\frac{d\theta}{dt}\right)_{sym}\right]_{20}. \tag{6.10}$$

b. The geopotential field between 0 and 20^{o}N is changed to satisfy the linear balance equation

$$\nabla^2\phi_{new} = \nabla\cdot(2\Omega\sin\theta\ \nabla\psi) \tag{6.11}$$

with the boundary conditions

$$\theta = 0: \quad \partial\phi_{new}/\partial\theta = 0. \tag{6.12}$$

$$\theta = 20^{o}\text{N}: \quad \phi_{new} = \phi_{sym}\ . \tag{6.13}$$

c. Values of the zonal and meridional velocity components and ϕ at the Southern Hemisphere latitudes -2.5^{o}, -5^{o}, etc., are set equal to the appropriately symmetrical values from the corresponding Northern Hemisphere latitudes $+2.5^{o}$, $+5^{o}$, etc.

At this point, the zonal and meridional velocities ($a\cos\theta\ d\lambda/dt$) and ($a\ d\theta/dt$) on the now symmetrical GLOPEP data set are rotated into the stereographic components u and v by use of eq (2.5), (2.6), and (1.10).

Each forecast grid array A, B, and C is characterized by its own i and j ranges:

$$i = 1,2,\ldots,IM,$$

$$j = 1,2,\ldots,JM.$$

It also has its own pole coordinates, i_p and j_p, valid for the H points of the Eliassen scheme of figure 2.1. (The determination of i_p and j_p for grids B and C is described in Appendix H.) Each forecast grid array is now filled with the variables H, Hθ, Hq, Hu, and Hv as follows:

a. For each i and j gridpoint, x and y for the H point are equal to

$$x = (i - i_p)\cdot\Delta \tag{6.14}$$

$$y = (j - j_p)\cdot\Delta. \tag{6.15}$$

For the associated Hu (Hv) points with the same i,j subscripts (see figure 4.1), eq (6.15) (or (6.14)) is increased by 0.5Δ. Δ in these formulae is of course the value appropriate to the grid in question as defined in eq (1.7), (1.8), and (1.9). These values of (x,y) define the (Greenwich) longitude by means of eq (1.10) and a relation derived from (1.5):

$$\rho = (x^2 + y^2)/4a^2, \tag{6.16}$$

$$\theta = \sin^{-1}\left(\frac{1-\rho}{1+\rho}\right). \tag{6.17}$$

b. Using these three pairs of values of $(\lambda,\theta)_{ij}$, a modified bilinear horizontal interpolation on the GLOPEP array is used to get 12 isobaric values of ϕ, u, and v, and six isobaric values of relative humidity as these are needed in steps d, e, f, and g below. A value of surface geopotential ϕ_g is also interpolated from the 1^o x 1^o data set described earlier in this chapter.

c. Current sea surface temperature values and Cressman drag coefficients, which are tabulated on a stereographic grid at NMC, are obtained by interpolation.

d. Surface pressure H is determined from ϕ_g and the column of isobaric ϕ values as follows. Let $\overline{\phi}(p)$ denote the geopotential in a standard atmosphere. When $\phi_g < \phi$ at 85 cb, the analyzed values of ϕ at 100, 85, and 70 cb are used to define a quadratic fit of ϕ to $\overline{\phi}$. This quadratic is inverted to determine the $\overline{\phi}$ appropriate to ϕ_g, and this $\overline{\phi}(p)$ is then converted into a pressure value. When ϕ_g is greater than ϕ at 85 cb, the same procedure is used with a cubic fit to $\overline{\phi}$ from the analyzed ϕ at the two pressure levels whose $\overline{\phi}$ is below ϕ_g and the two pressure levels whose $\overline{\phi}$ is above ϕ_g.

e. The prescribed $\Delta\sigma$ values determine $\hat{p}_k$ at the interfaces according to eq (1.1). The pressure p_k in the layers is defined in the NGM by

$$(p_k)^{\kappa} = \frac{\hat{p}_k^{\,1+\kappa} - \hat{p}_{k+1}^{\,1+\kappa}}{(1+\kappa)(\hat{p}_k - \hat{p}_{k+1})}, \tag{6.18}$$

where $\kappa = R/c_p$. (See the discussion in Appendix A.) The hydrostatic equation can be rewritten, again using $\overline{\phi}(p)$ as the "pressure" variable, in the form

$$\frac{d\phi}{d\overline{\phi}} = \frac{T(p)}{\overline{T}(p)} \equiv \tau(p). \tag{6.19}$$

This is used to define 11 τ's (ℓ = 1 to 11) located at the 11 $\overline{\phi}_\ell$ values midway (in $\overline{\phi}$) between the 12 standard pressure surfaces. p_k from eq (6.18) is converted to a $\overline{\phi}_k$ value. Then a value τ_k is assigned to this layer, equal to $\tau_{\ell=1}$ if $\overline{\phi}_k < \phi_{\ell=1}$, equal to $\tau_{\ell=11}$ if $\overline{\phi} \geq \overline{\phi}_{\ell=11}$, and equal to the appropriate weighted mean of τ_ℓ and $\tau_{\ell+1}$ when $\phi_\ell < \phi_k \leq \phi_{\ell+1}$. τ_k is converted to T_k by multiplication with $\overline{T}(p_k)$ and then multiplied by (H/π_k) to give $H\theta_k$.

f. The six relative humidity values on GLOPEP are first extended up to 5 cb by linearly extrapolating the 30 cb value to zero at 5 cb. These are interpolated to the sigma layer pressure values and multiplied by the saturation specific humidity appropriate to p_k, T_k. Zero is used for q when $p_k < 5$ cb. Values of q greater than 0.9 of q (saturation) are reduced to that value. [See the discussion following eq (4.12).]

g. After the atmospheric variables H, Hθ, and Hq have been filled in for a grid, the Hu and Hv arrays are filled in. The H values needed at the Hu and Hv points are given by the appropriate 2-point average of the nearest two H points (figure 2.1) and then are used to give the layer pressure values, p_k. Simple vertical interpolation is used to get u_k and v_k. When $p_k < 5$ cb, u_k and v_k are set equal to the 5-cb value.

The meteorological aspect of the initial gridpoint fields determined in this way is not completely satisfactory. One obvious bias is the interpretation of virtual temperatures as actual temperatures. Other defects are not due to the interpolation procedures described above, but are inherent in the input global analyses. From experience with about 10 cases, they can be summarized as follows:

1. Although the wind field $\vec{v}$ is in satisfactory geostrophic balance with ϕ, the "cyclostrophic correction," present in the upper troposphere in sharp troughs, is weak.

2. Sharp jets (over North America where the data are dense) are often broader than justified by the data (Phillips 1977).

3. The detail of the sloping stable layers of strong fronts is missing (Phillips 1977).

4. Low-level inversions are smoothed vertically; temperatures in the bottom sigma layers are often too warm by several degrees. This (and point 3) is presumably due to reliance on standard pressure geopotentials to derive T(p).

5. The Flattery humidity analyses tend to be too moist in the lower troposphere.

6. It is suspected that the wind analyses at low levels (100 or 85 cb) do not adequately reflect frictional effects in the observations.

An example of forecast sensitivity to analysis is shown in figures 6.1, 6.2, and 6.3, the East Coast snowstorm of February 1978 (Brown and Olson 1978). The two 48-hr NGM forecasts shown on figures 6.2 and 6.3 were made in a 10-level 2-grid format with grid B centered over North America with a horizontal resolution of 198 km at 45^{o}. The forecast in figure 6.2 used the Flattery initial data as described above. It fails to indicate the Cape Hatteras Low shown on figure 6.1. The forecast shown in figure 6.3 used the Cressman analysis (that is made for the LFM model) instead of the Flattery analysis, in the LFM area. The Hatteras Low is now predicted well. The two 48-hr 500-mb forecasts also differed noticeably, with the LFM analysis again producing a better result. In this case it appears that the 1200Z 4 February Flattery analysis had too smooth a vorticity pattern at 500 mb and too broad a thermal gradient in the Minnesota-James Bay region.

Output procedures to give forecast grids on constant pressure surfaces from the NGM sigma fields are straightforward. The geopotential height of an isobaric surface is computed from the ground geopotential ϕ, surface pressure H, and sigma layer θ values, by treating them as the equivalent of a (dry) radiosonde ascent.

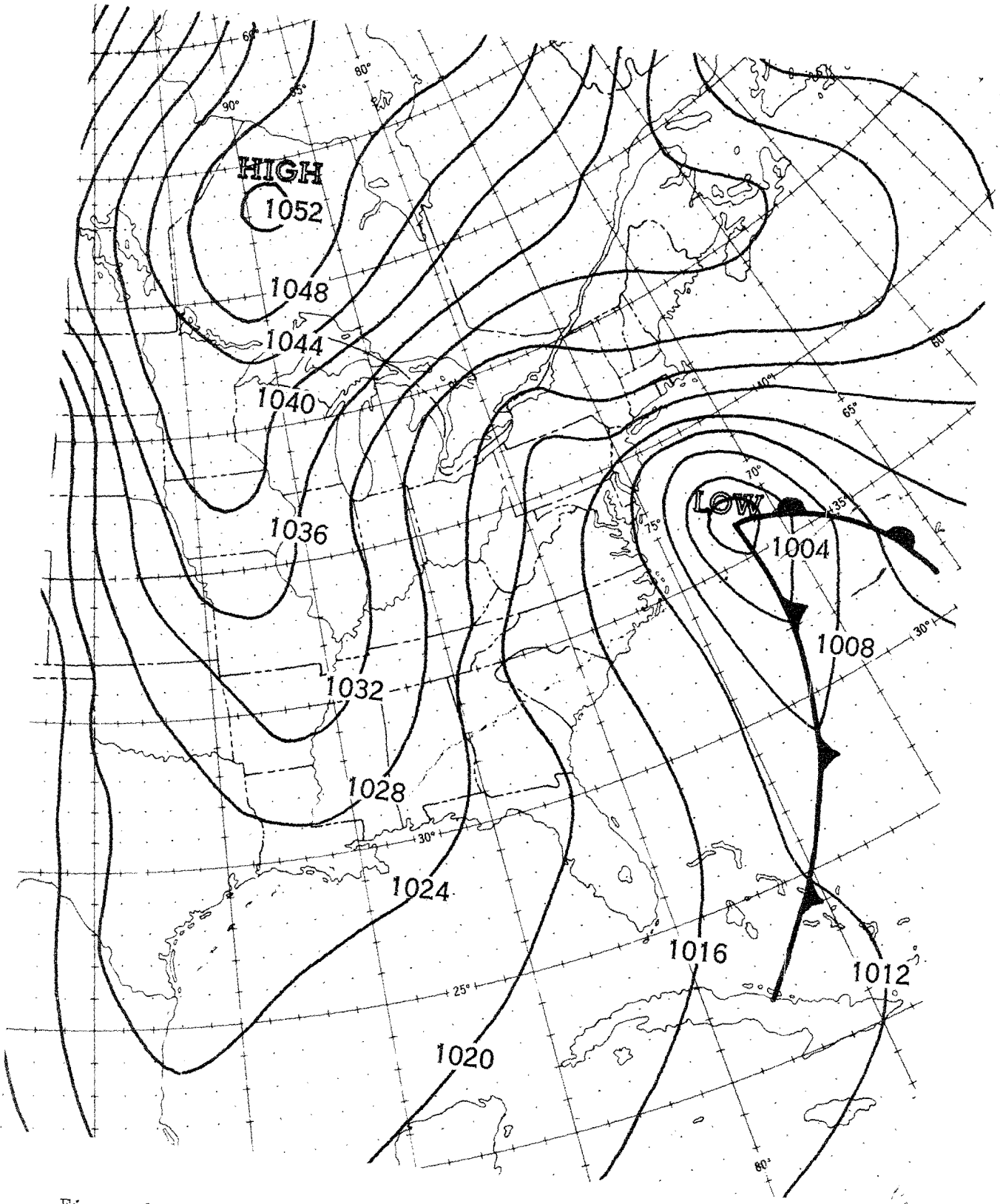

Figure 6.1.--Sea level verifying chart at 1200 GMT 6 February 1978.

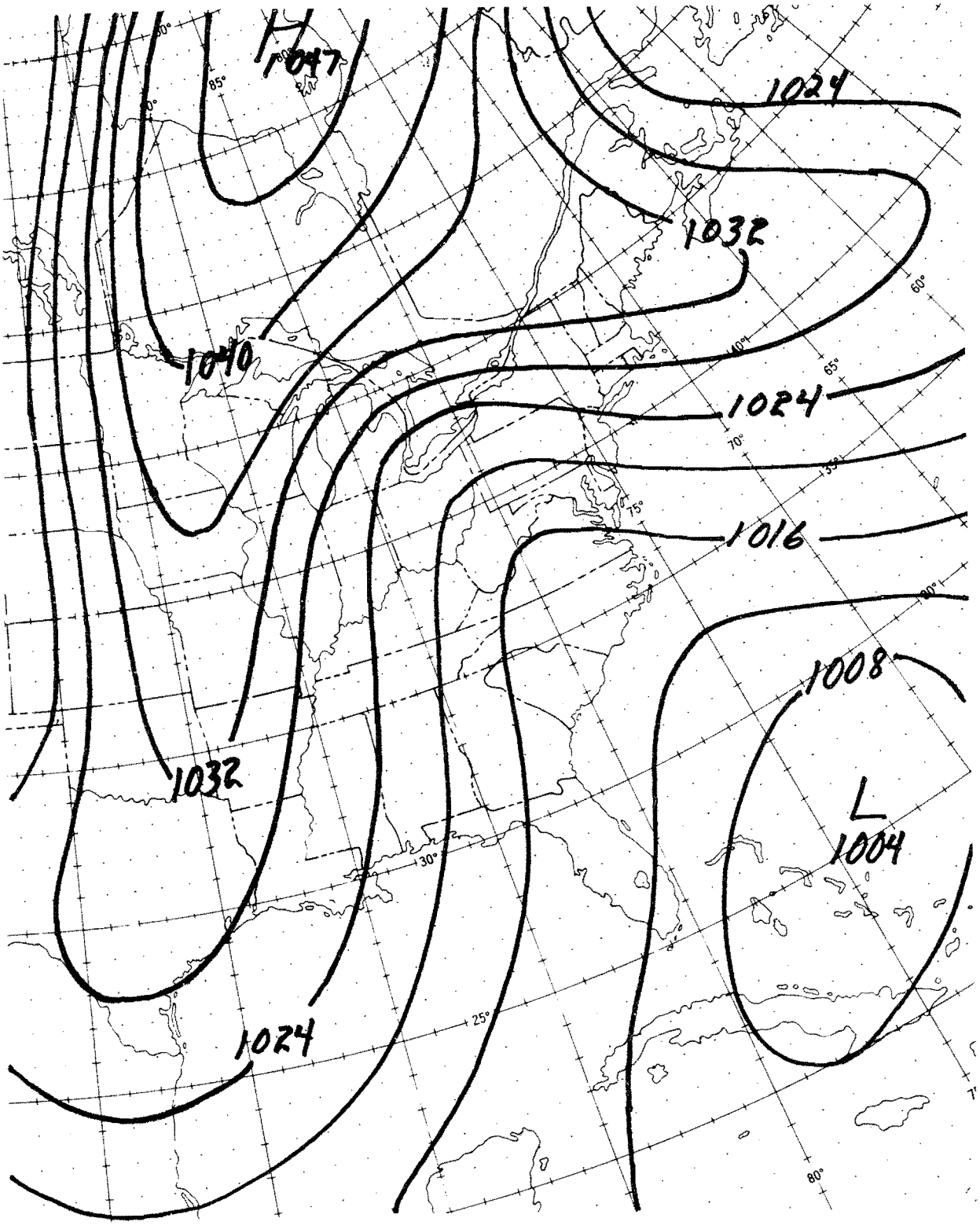

Figure 6.2.--48-hr NGM forecast made from Flattery analysis.

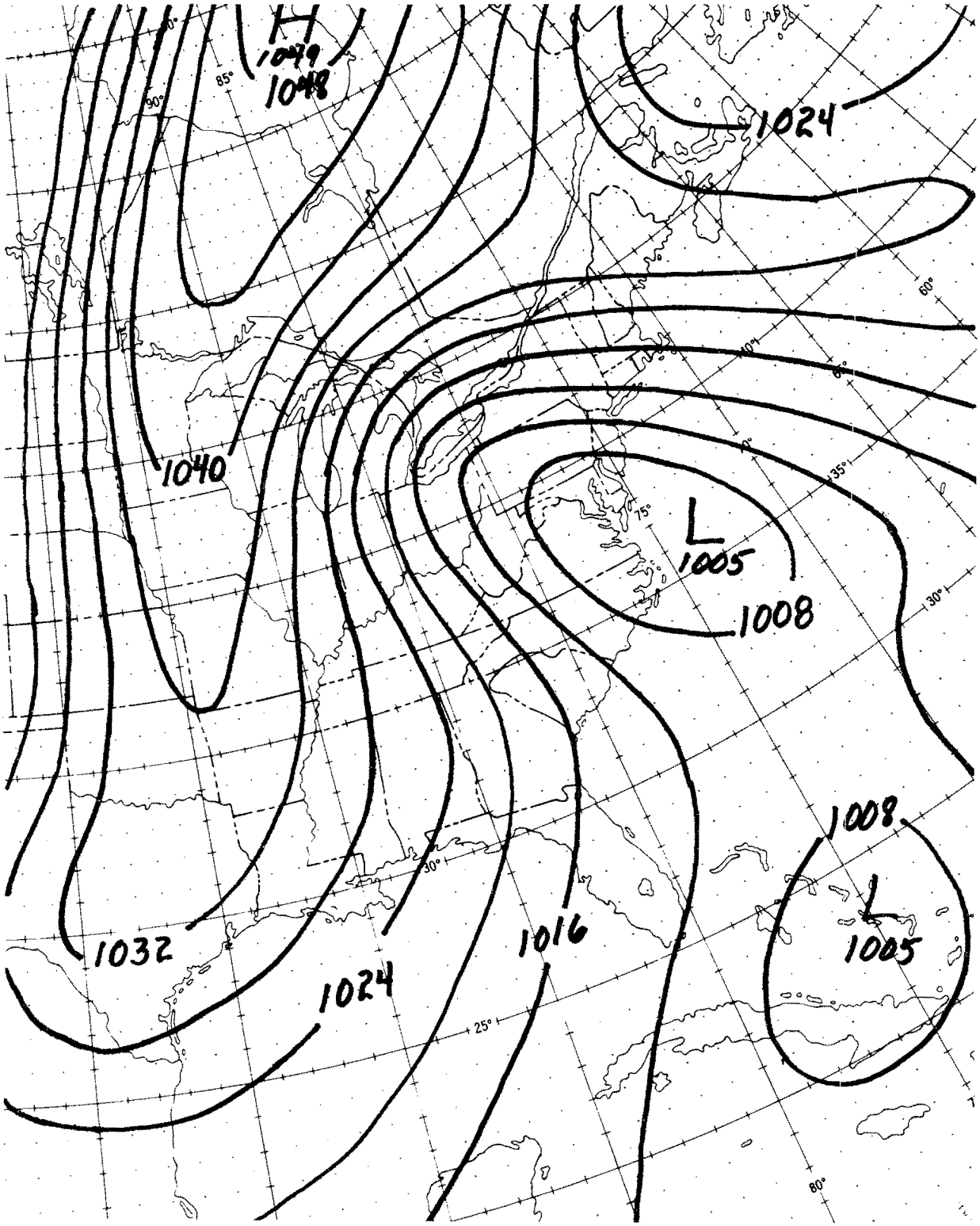

Figure 6.3.--48-hr NGM forecast made using Cressman (LFM) analysis over North America.

CHAPTER VII: HIMALAYAN TREATMENT

As mentioned in Chapter IV, the combination of steep orography and a sharp tropopause gives rise to errors in the σ-coordinate evaluation of the horizontal pressure force:

$$(\nabla\phi)_p = \nabla\phi + c_p\theta\nabla\pi. \tag{7.1}$$

This is a truncation error. Experience with varying horizontal resolution in the NGM over the Himalayas has shown that when the horizontal grid increments are not larger than several hundred kilometers, it is vertical truncation error which is most serious.

The vertical character of this truncation error may be demonstrated as follows. For simplicity in this demonstration, we use

$$Z = -\ln p = -\ln[H(1 - \sigma)] \tag{7.2}$$

as the vertical pressure coordinate, so that the hydrostatic equation becomes

$$\frac{d\phi}{dZ} = RT, \tag{7.3}$$

and the pressure force in the sigma system is

$$F = \nabla\phi + RT\ \nabla\ \ln H. \tag{7.4}$$

Consider now the special case of ϕ and T varying only with pressure (i.e., Z):

$$T = T(Z), \quad \phi = \phi(Z), \tag{7.5}$$

so that eq (7.4) should equal zero.

If the hydrostatic relation eq (7.3) is integrated in a simple second-order fashion using equal intervals ΔZ in Z [i.e., equal intervals in $\ln(1 - \sigma)$], the result is

$$\phi_{k+1} - \phi_k = \frac{R\cdot\Delta Z\cdot}{2}(T_k + T_{k+1}). \tag{7.6}$$

The difference in eq (7.4) at levels k+1 and k is then

$$F_{k+1} - F_k = \frac{R}{2}\ \Delta Z\ \nabla(T_k + T_{k+1}) + R(T_{k+1} - T_k)\nabla\ \ln H. \tag{7.7}$$

But under the special condition eq (7.5) that T only varies with Z,

$$\nabla T_k = \left(\frac{dT}{dZ}\right)_k \nabla Z_k = -\left(\frac{dT}{dZ}\right)_k \nabla\ \ln H \tag{7.8}$$

(At this point we are ignoring horizontal truncation errors.) The result is

$$F_{k+1} - F_k = R \cdot \Delta Z \cdot \left[\frac{T_{k+1} - T_k}{\Delta Z} - \tfrac{1}{2}\left(\frac{dT}{dZ_k} + \frac{dT}{dZ_{k+1}} \right) \right] \nabla \ln H. \qquad (7.9)$$

If T_{k+1} and $(dT/dZ)_{k+1}$ are expanded in a Taylor series about level k, eq (7.9) reduces to

$$F_{k+1} - F_k = - \frac{R(\Delta Z)^3}{12} \left(\frac{d^3T}{dZ^3} \right)_k \nabla \ln H + O(\Delta Z^4) \qquad (7.10)$$

or, alternately,

$$F_{k+1} - F_k = - \frac{R(\Delta Z)^2}{12} \left[\left(\frac{d^2T}{dZ^2} \right)_{k+1} - \left(\frac{d^2T}{dZ^2} \right)_k \right] \nabla \ln H + O(\Delta Z^3). \qquad (7.11)$$

Since F_k should be zero under condition (7.5), this describes the vertical truncation error. Eq (7.10) and (7.11) illustrate the way in which large orographic slopes (which give large $\nabla \ln H$) and sharp changes in lapse rate combine to create this error.

The fictitious value of $(\nabla\phi)_p$ over the Himalayan slopes in the NGM can reach values near the tropopause as large as the value associated with a geostrophic wind of 10 m/s. These are not in balance with the initial windfield and thus create the gravity waves described in Chapter IV. Sundqvist (1976) has suggested that the initial ϕ field (actually the temperatures) be modified by requiring that the horizontal divergence of the right side of eq (7.1) or (7.4) at t = 0 be set equal to the horizontal divergence of the left side of those equations after the (correct) horizontal vector $(\nabla\phi)_p$ computed on pressure surfaces has been interpolated vertically to values on sigma surfaces. His procedure evidently reduces the amplitude of the ensuing gravity waves, but it gives rise to large changes in the stratospheric temperature field.

An alternate method used in the NGM initialization procedure is designed to ameliorate only the Himalayan source of these waves. This procedure requires the running of a preliminary 24-hr dry forecast on grid A. The initial data for this preliminary forecast has no velocities and zero specific humidity. Geopotentials everywhere on the input GLOPEP data set (Chapter VI) are replaced by 12 horizontally uniform values of ϕ, each equal to a regional average in the Himalayan area from a weather situation typical of the season for which forecasts are to be made.

A rectangular area (I) is defined on grid A, of size several thousand kilometers on a side, and centered over the Himalayas. A larger rectangular "buffer" zone (II) of width 1000 km is placed around area I. Twenty-four successive 1-hr forecasts are now made on grid A with this artificial initial condition. At the end of each hour, the gridpoint values outside of the buffer zone are set back to their initial value. No change is made to the forecast values in area I, but the forecast values in the buffer zone are progressively modified toward the $t = 0$ value, proportional to the closeness of the buffer zone gridpoint to area I or to the outer boundary of the buffer zone. The forecast for the next hour is then made. Gravity waves are sent out by the Himalayas in this process, but the repeated reinitialization in the external region removes them from the forecast there while allowing the variables in the Himalayan region to adjust to the incorrectly computed pressure force. The 24-hr forecast changes in $H\theta$, Hu, Hv, and H in areas I and II of this grid A are then saved for reference, and are simply added to the grid A initial values whenever a forecast is to be made (in the same season) with a model having the same horizontal gridpoint structure of grid A (i.e., the same value of NH) and the same vertical distribution of σ layers.

Velocity and potential temperature changes as large as 20 m/s and 10^{o} are produced in this way over the Himalayan slopes near the tropopause. These changes are large enough to be unattractive from the viewpoint of forecasting in the Himalayan region, but essentially the same changes would occur there during the regular NGM forecast even if this special initialization were not done. Outside of the Himalayas, the major travelling oscillation from the Himalayas shown on figure 4.1 is reduced by a factor of 3 or more.[1]

---

[1]The nonlinear normal mode initialization procedures being developed by Machenhauer (1977), Baer (1977), and Daley (1978) would presumably accomplish this balancing more expeditiously and on a global basis for all orography. However, it, as well as the Sundqvist treatment and the NGM treatment described here, are only palliatives because they do not basically reduce the error eq (7.10).

CHAPTER VIII: COMPUTATIONAL STABILITY AND TRUNCATION ERROR

The computational stability of linearized forms of the continuous equations given in Chapter II (and their finite-difference equivalents in Appendices A-F) can be approached in the usual manner by first separating out the vertical variation of the linearized equations. In this first step, the linear equations are

$$\frac{\partial \vec{v}_k}{\partial t} = - \nabla\phi_k - \overline{RT}_k \nabla h - f\,\hat{k} \times \vec{v}_k, \tag{8.1}$$

$$\frac{\partial \theta_k}{\partial t} = - \frac{1}{2\Delta\sigma_k}\left[w_{k+1}(\overline{\theta}_{k+1} - \overline{\theta}_k) + w_k(\overline{\theta}_k - \overline{\theta}_{k-1})\right], \tag{8.2}$$

$$w_{k+1} - w_k = - \Delta\sigma_k \left(\frac{\partial h}{\partial t} + \nabla\cdot\vec{v}_k\right), \tag{8.3}$$

$$\phi_1 = c_p\, \overline{H}^{\kappa} \sum_{k=1}^{K} T\, W_k[\theta_k + (\kappa\, \overline{\theta}_k)h], \tag{8.4}$$

$$\phi_k - \phi_{k-1} = c_p\, \overline{H}^{\kappa}(PR_{k-1} - PR_k)[(\theta_k + \theta_{k-1}) + \kappa(\overline{\theta}_k + \overline{\theta}_{k-1})h]. \tag{8.5}$$

ϕ_k, $\vec{v}_k$, θ_k are the perturbations of geopotential, wind, and potential temperature, w is $d\sigma/dt$, and h is the perturbation of $\ell n(H)$. Basic state variables are denoted by $\overline{H}$, $\overline{\theta}_k$ and $\overline{T}_k = \overline{p}_k^{\kappa}\,\overline{\theta}_k$. TW_k and PR_k are the fixed functions of σ defined in Appendix A. The vertical boundary conditions are that w_k vanish at k = 1 and K + 1. Separation of variables is achieved by assuming that ϕ_k, θ_k, and h are each equal to a function of k times the same function $\Phi(x,y,t)$, that w_k is equal to a function of k times $\partial\Phi/\partial t$, and that $\vec{v}_k$ is equal to a function of k times $\vec{V}(x,y,t)$. Φ and V are related by the familiar equations

$$\frac{\partial \vec{V}}{\partial t} = - \nabla\Phi - f\,\vec{k} \times \vec{V} \tag{8.6}$$

$$\frac{\partial \Phi}{\partial t} = - c^2 \nabla\cdot\vec{V}. \tag{8.7}$$

c^2 is a separation constant, inversely proportional to one of the K eigenvalues of the matrix arising from requiring compatibility of the four functions of k introduced above with the vertical structure of eq (8.1)-(8.5).[1]

Sample results of the vertical eigenvalue problem are shown here for a model with 10 layers defined by the $\Delta\sigma$'s tabulated in eq (1.4). The basic state is a tropical-like atmosphere characterized by a surface pressure of 102.5 cb, a surface temperature of 302K, a linear decrease of T with (- ℓn p) to a tropopause of 191K at 10 cb, and a stratosphere in which T increases linearly with (- ℓn p) to a value of 273K at p = 0.09 cb. The 10 values of $\sqrt{c^2}$ are listed in table 8.1, together with the vertical distribution of

$$\hat{\omega}_k = \frac{d\hat{p}}{dt} = \hat{\overline{p}}_k \frac{\partial h}{\partial t} - \overline{H}\, w_k \qquad (8.8)$$

from the eigenvectors associated with each value of c^2.

The well-known decrease of c with increasing number of sign changes in the ω eigenvectors is clear. The "external gravity" (or "Lamb wave") mode has c = 313 m/s, a very reasonable value. Its ω varies like p to the 0.89 power in the troposphere, somewhat more rapidly than the p to the 0.71 power dependence of ω in the Lamb wave of an infinite isothermal atmosphere. At the higher wavenumber end, however, the effect of vertical truncation error is pronounced. For example, the 10th mode in table 8.1, with its c = 1 m/s, has a tropospheric vertical wavelength L_z of about 3000 meters.

---

[1]Several properties of the matrix may be of interest.

(a) In the special case of complete adiabatic stratification ($\overline{\theta}_k$ = constant), there are K-1 multiple eigenvalues $c^2 = 0$, and the Kth root is $c^2 = RT_{ground}$. The latter agrees with the single discrete eigenvalue that exists in the continuous adiabatic case.

(b) If two adjacent layers have equal $\overline{\theta}$, one solution will have $c^2 = 0$. Its eigenvector will have a zero value for the surface pressure perturbation (h), and a nonzero w only at the interface located between the two equal $\overline{\theta}$ values.

I have been unable to extend (b) to prove the intuitive expectation that there will be one negative c^2 if and only if $\overline{\theta}_{k+1} < \overline{\theta}_k$ for one value of k. Numerical tests verify this conjecture, but algebraic proof has so far eluded me.

Table 8.1.--Square root of eigenvalues ($\sqrt{c^2}$) in m/s and eigenvectors for dp/dt at interfaces of indicated pressure (cb), normalized to a nominal maximum of 100 for a 10-layer NGM. Values of $\sqrt{c^2}$ for a 16-layer model are listed in parentheses.

	$\sqrt{c^2}$									
p	313 (313)	144 (168)	54 (62)	27 (39)	17 (26)	11 (17)	8 (12)	5 (9)	3 (7)	1 (6)
7.2	10	83	-7	3	-2	2	-1	2	-1	-0
15.2	18	100	28	-41	61	-62	47	-61	37	10
24.4	28	91	69	-63	28	18	-44	78	-55	-16
35.6	39	75	96	-23	-67	61	3	-67	63	21
51.2	54	48	100	61	-55	-75	61	31	-69	-32
66.9	68	20	79	100	58	-37	-93	33	78	55
78.1	78	+0	55	89	100	67	-17	-92	-54	-88
87.3	87	-17	32	61	86	100	100	23	-40	100
95.3	94	-31	10	28	45	63	92	100	100	-73
102.5	100	-44	-9	-4	-2	-1	-1	-1	-0	+0

The simple approximate formula for internal gravity waves

$$c^2 = \frac{N^2 L_z^2}{4\pi^2} \tag{8.9}$$

where $N = g\, d\ell n\, \overline{\theta}/dz \sim 10^{-4}\ s^{-2}$, would for this L_z give a value for c of about 6 m/s. The table also contains the 10 largest values of $\sqrt{c^2}$ from a 16-layer model, and demonstrates clearly the slowness of the highest order modes of the 10-level results. This excessive smallness of c for the high-order internal waves is probably due to the vertical averaging of w and θ that exists on the r.h.s. of eq (8.2) and (8.5).

The second mode (c = 144 m/s) is unique in having its largest ω value near the very cold tropopause located at 100 mb. The associated horizontal velocity eigenfunction has an almost uniform positive value in

the eight layers below 15.2 cb, changing suddenly to a large negative value in the top two layers of the model. (It is therefore much like an internal long gravity wave on the surface of separation between two homogeneous incompressible fluids of different densities.) This mode has a less extreme structure, however, in basic states having warmer tropopause at a lower elevation and a less stable stratosphere.

The horizontal part of the computational stability problem is attacked by applying the Eliassen staggered grid of figure 2.1 and the detailed Lax-Wendroff double-step procedure of Appendices B-F to the separated eq (8.6) and (8.7). The effect of horizontal advection is reincorporated by adding a uniform basic current (u_o, v_o) in the (x,y) directions, so that $\partial/\partial t$ in eq (8.6) and (8.7) is replaced by

$$\frac{\partial}{\partial t} + u_o \frac{\partial}{\partial x} + v_o \frac{\partial}{\partial y} . \tag{8.10}$$

The perturbation variables $(u,v) = \vec{V}$, and Φ are assumed to have the forms

$$\begin{aligned} u_{pqn} &= c\, U_n\, \psi_{pq}\, \exp(i\beta/2) \\ v_{pqn} &= c\, V_n\, \psi_{pq}\, \exp(i\alpha/2) \\ \Phi_{pqn} &= c^2 H_n\, \psi_{pq} \end{aligned} \tag{8.11}$$

where

$$\psi_{pq} = \exp\, i(\alpha p + \beta q). \tag{8.12}$$

p and q have replaced i and j as horizontal gridpoint numbers for notational clarity:

$$x = p\Delta, \quad y = q\Delta, \quad t = n\Delta t, \tag{8.13}$$

and α and β are measures of the horizontal wavenumber.

The analysis proceeds exactly as described in Phillips (1962, see page 114), except that the half time step advection operation described in Appendix E is slightly simpler than the interpolation process described in the above reference. The result is that the vector of amplitude coefficients

$$Z_n = \begin{pmatrix} U_n \\ V_n \\ H_n \end{pmatrix} \tag{8.14}$$

obeys the law

$$Z_{n+1} = A\, Z_n \tag{8.15}$$

in which the matrix A is defined by

$$A = I - 2G(i\delta I + G). \tag{8.16}$$

I is the 3 x 3 identity matrix, and

$$\delta = \cos\frac{\alpha}{2}\cos\frac{\beta}{2}. \tag{8.17}$$

The 3 x 3 matrix G is given by

$$G = \begin{pmatrix} W & iF & M \\ -iF & W & N \\ M & N & W \end{pmatrix} \tag{8.18}$$

in which the symbols denote

$$F = f\Delta t/2, \tag{8.19}$$

$$W = \sigma[\cos\chi \sin\frac{\alpha}{2}\cos\frac{\beta}{2} + \sin\chi \cos\frac{\alpha}{2}\sin\frac{\beta}{2}], \tag{8.20}$$

$$M = \mu \sin\alpha/2 \tag{8.21}$$

$$N = \mu \sin\beta/2 \tag{8.22}$$

$$(u_o, v_o) = |\vec{V}_o| \ (\cos\chi, \sin\chi) \tag{8.23}$$

$$\sigma = |\vec{V}_o| \ \Delta t/\Delta \tag{8.24}$$

$$\mu = c \ \Delta t/\Delta \tag{8.25}$$

(χ is the direction of the basic current.)

The three eigenvalues of A are, for $\ell = 1, 2, 3$:

$$\lambda_\ell = 1 - 2\,\gamma_\ell(i\delta + \gamma_\ell), \tag{8.26}$$

where γ_ℓ are the eigenvalues of G

$$\gamma_1 = W, \tag{8.27}$$

$$\gamma_2 = W - (F^2 + M^2 + N^2)^{\frac{1}{2}}, \tag{8.28}$$

$$\gamma_3 = W + (F^2 + M^2 + N^2)^{\frac{1}{2}}. \tag{8.29}$$

It is shown in Phillips (1962) how the F^2 terms may be ignored in assessing the von Neumann computational stability criterion

$$|\lambda|_{max} \leq 1 + 0(\Delta t). \tag{8.30}$$

The resulting requirement for stability is that

$$[W + (M + N)^{\frac{1}{2}}]^2 + \delta^2 \leq 1 . \tag{8.31}$$

The maximum of W for arbitrary direction χ is $\sigma(a + b - 2ab)$, where a and b are defined as

$$a = \sin^2(\alpha/2), \tag{8.32}$$

$$b = \sin^2(\beta/2). \tag{8.33}$$

This allows eq (8.31) to be written as

$$\sigma\left(\frac{a + b - 2ab}{\sqrt{a + b - ab}}\right) + \mu\left(\frac{a^2 + b^2}{\sqrt{a + b - ab}}\right) \leq 1. \tag{8.34}$$

Separate maximization of the two factors gives the sufficient condition $\sigma + \sqrt{2}\mu \leq 1$. However, numerical exploration of eq (8.34) as a function of a and b shows that the more generous condition

$$\text{For } \sigma < 1 - \frac{1}{\sqrt{2}}: \quad \mu \leq \frac{1}{\sqrt{2}} , \tag{8.35}$$

$$\text{For } 1 - \frac{1}{\sqrt{2}} \leq \sigma \leq 1: \quad \mu \leq 1 - \sigma, \tag{8.36}$$

is allowed. This is graphed in figure 8.1.

A brief comparison with the Shuman (1962) "semimomentum" finite-differencing treatment of eq (8.6), (8.7) is worth recording. That system (see also Gerrity 1977, pp. 18-20) leads to linearized finite-difference solutions of the form $\exp i(\alpha p + \beta q - \theta n)$ where $\sin\theta$ is equal to

$$\sigma[\cos\chi \sin\alpha(1-b) + \sin\chi \sin\beta(1-a)] \tag{8.37}$$

for the advective wave, and to the sum of eq (8.37) and

$$\pm 2[F^2(1-a)^2(1-b)^2 + \mu^2(1-a)(1-b)(a+b-2ab)]^{\frac{1}{2}} \tag{8.38}$$

for the gravity waves.[1] Computational stability of this system requires $|\sin\theta| \leq 1$ which leads ultimately to

$$\sigma + \mu = \left(c + |\vec{V}_o|\right)\frac{\Delta t}{\Delta x} \leq 1. \tag{8.40}$$

---

[1]Computational modes in which $-\theta$ is replaced by $\theta+\pi$ are also present due to the leapfrog aspect of the Shuman method.

This condition is more generous than eq (8.35)-(8.36) for $c > (1+\sqrt{2})\ |\vec{V}_o|$ (fig. 8.1).

In application, μ in these criteria will be set by the largest c value ($\sim$313 m/s) and σ by the largest expected windspeed, which we will take as 100 m/s. This combination occurs on the line $\mu = 3.13\sigma$ in figure 8.1. For the Lax-Wendroff system this intersects with the line $\mu = 1/\sqrt{2}$, so that the effective criterion is determined by μ only:

$$\Delta t_{LW} \leq \frac{\Delta}{\sqrt{2}c_{max}} = 0.71\ \frac{\Delta}{c_{max}} \tag{8.40}$$

For eq (8.39), the critical value is

$$\Delta t_s \leq \frac{313}{413}\ \frac{\Delta}{c_{max}} = 0.76\ \frac{\Delta}{c_{max}}\ . \tag{8.41}$$

The extra stability region in the Shuman scheme is therefore of little practical significance.

Δ in these formulas is the horizontal <u>distance</u> increment, equal to the finite difference mesh size divided by the map factor m. This means that for a hemispheric polar stereographic region, the effective Δ is that at the Equator. In the NGM, the uniform ratio Δt/(mesh size) for all three grids means that it is the outer grid A (at the Equator) that sets Δt because it has there the smallest value of (Δt/distance increment) found in the complete NGM grid system.

An interesting comparison is that of the ratio of the computational frequency to the true frequency for the Shuman method and the Lax-Wendroff method. For this comparison we assume a Δt equal to 0.9 of the maximum values eq (8.40) and (8.41), c = 310 m/s, $|\vec{V}_o|$ = 25 m/s, $\chi = 45^o$, and equality of the x and y wavenumbers:

$$\alpha = \beta = \frac{2\pi}{N} = \frac{1}{\sqrt{2}}\ \frac{2\pi\Delta}{L} = \frac{2\pi}{N'}\ \frac{1}{\sqrt{2}}$$

($\vec{V}_o$ is now in the direction of the two-dimensional wavenumber vector.) N is the number of grid increments in one wavelength in the x and y direction; the number of grid increments in one two-dimensional wavelength is then $N' = N/\sqrt{2}$. Table 8.2 contains these results. (For simplicity, advection and Coriolis force have been ignored in the gravity wave formulas.) The advection wave ratios for the two systems agree extremely close. The Eliassen staggered Lax-Wendroff system, however, does a better job of moving gravity waves--a not-unexpected reward for the additional arithmetic it requires.

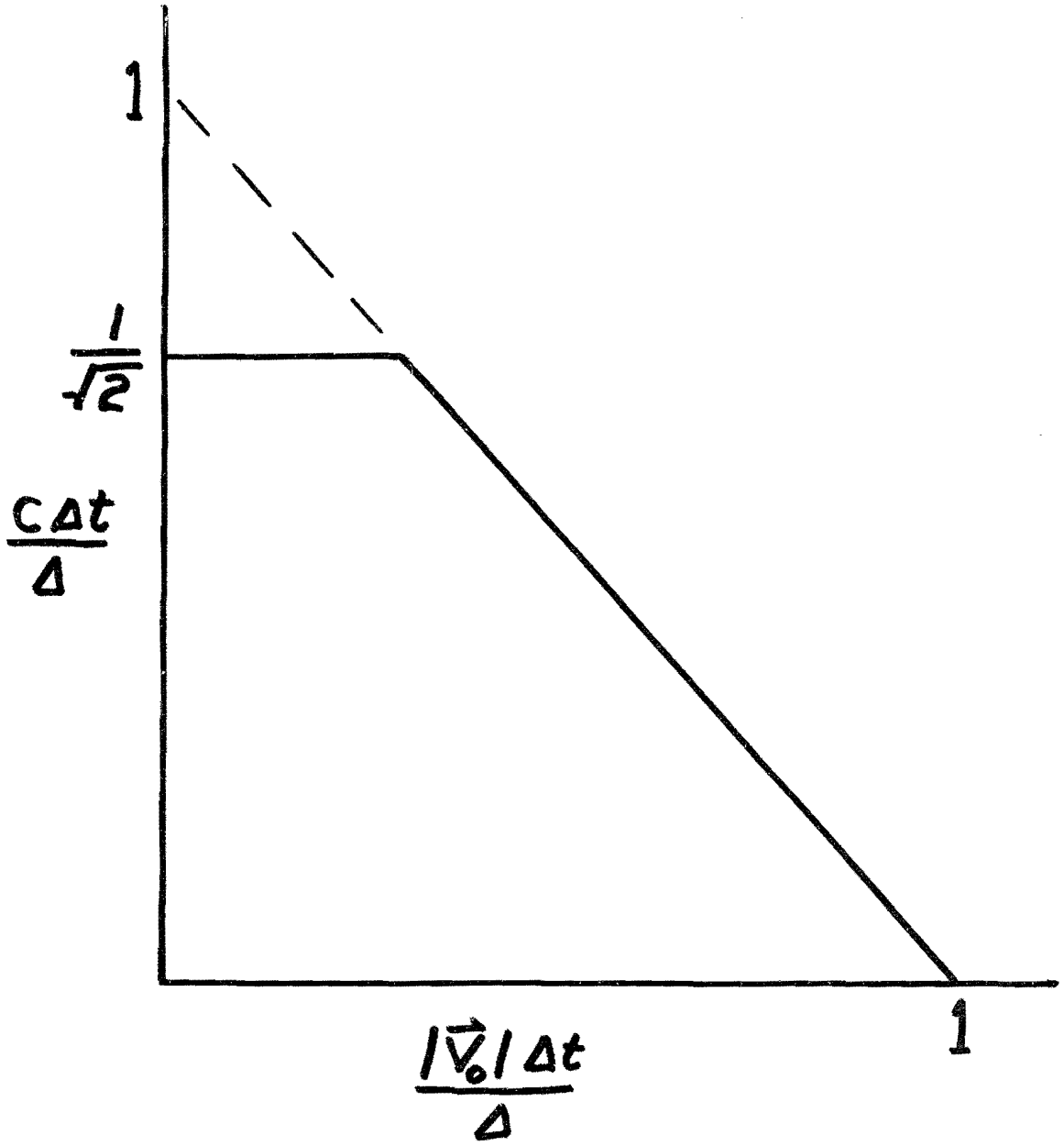

Figure 8.1.--Computational stability diagram. The NGM is stable within the truncated triangle; the Shuman scheme is stable for the complete triangle.

Table 8.2.--Ratio of the computational frequency to the true frequency for advective waves and pure gravity waves in the Shuman (S) and in the Lax-Wendroff (LW) schemes. (See text for details.)

N(N′)	Advective		Gravity	
	S	LW	S	LW
2 (1.4)	0.000	0.000	0.000	0.000
3 (2.1)	.103	.104	.104	.550
4 (2.8)	.318	.319	.336	.911
5 (3.5)	.496	.496	.541	.891
6 (4.2)	.621	.621	.684	.902
8 (5.7)	.769	.769	.834	.930
10 (7.1)	.846	.847	.899	.950
12 (8.5)	.891	.891	.932	.963
20 (14.1)	.960	.960	.977	.985

CHAPTER IX: SUMMARY OF RESULTS FROM NGM FORECASTS

About 10 forecasts out to 48 hr have been made with the NGM and have produced the following informative experimental results:

a. Cross-contour flow

The original NMC hemispheric operational primitive-equation model (the six-level Shuman-Hovermale model) often predicted the isotachs of the jet stream on the west side of a trough to cross the geopotential contours toward high values in a very unrealistic manner. In early 1976 the NGM was applied to a strong example of this phenomenon. When done on the grid A format alone (with NH = 30, roughly equal to the six-level model's horizontal resolution), the NGM had a similar problem. But when a grid B was added to the NGM, the error was eliminated. This strong hint that improved horizontal resolution would correct this error was a major factor in developing a finer resolution version of the hemispheric model at NMC (the seven-level model now in operational use).

b. Locked-in error

This is a large flow pattern error that often occurs in the NMC hemispheric (both six-level and seven-level) models and in the LFM, when the initial situation contains a trough over the western United States. The 36- and 48-hr forecasts from these models predict the 500-mb vorticity maximum too far south in the Mississippi valley, with a corresponding error in the position of the 1000-mb Low center. Increased horizontal resolution in these models has not made major improvements in this error.[1] The NGM has been run on four cases of this nature, with excellent results. The most pronounced example of this error found in the NGM among these four cases is illustrated in figure 9.1 for the case of 00Z 19 Nov. 1977. The NGM forecast used here had 10 levels. Essentially the same NGM forecast resulted when these 10 levels in the NGM were reduced to seven in number, with the seven $\Delta\sigma$'s chosen to be similar to those of the seven-layer NMC operational model. In a separate test, the special Arakawa hydrostatic relation used in the NGM (Appendix B) was replaced by a local formula for the geopotential difference between layer one and the ground (it being thought that form drag from the Rockies might be relevant). This change in the NGM also failed to increase the NGM forecast error. These results point toward some subtle failing of the horizontal finite differences used in the NMC hemispheric and LFM models.

---

[1]A somewhat more substantial reduction in this error has been achieved by a fourth-order semi-implicit model (Campana 1977) with a different grid structure.

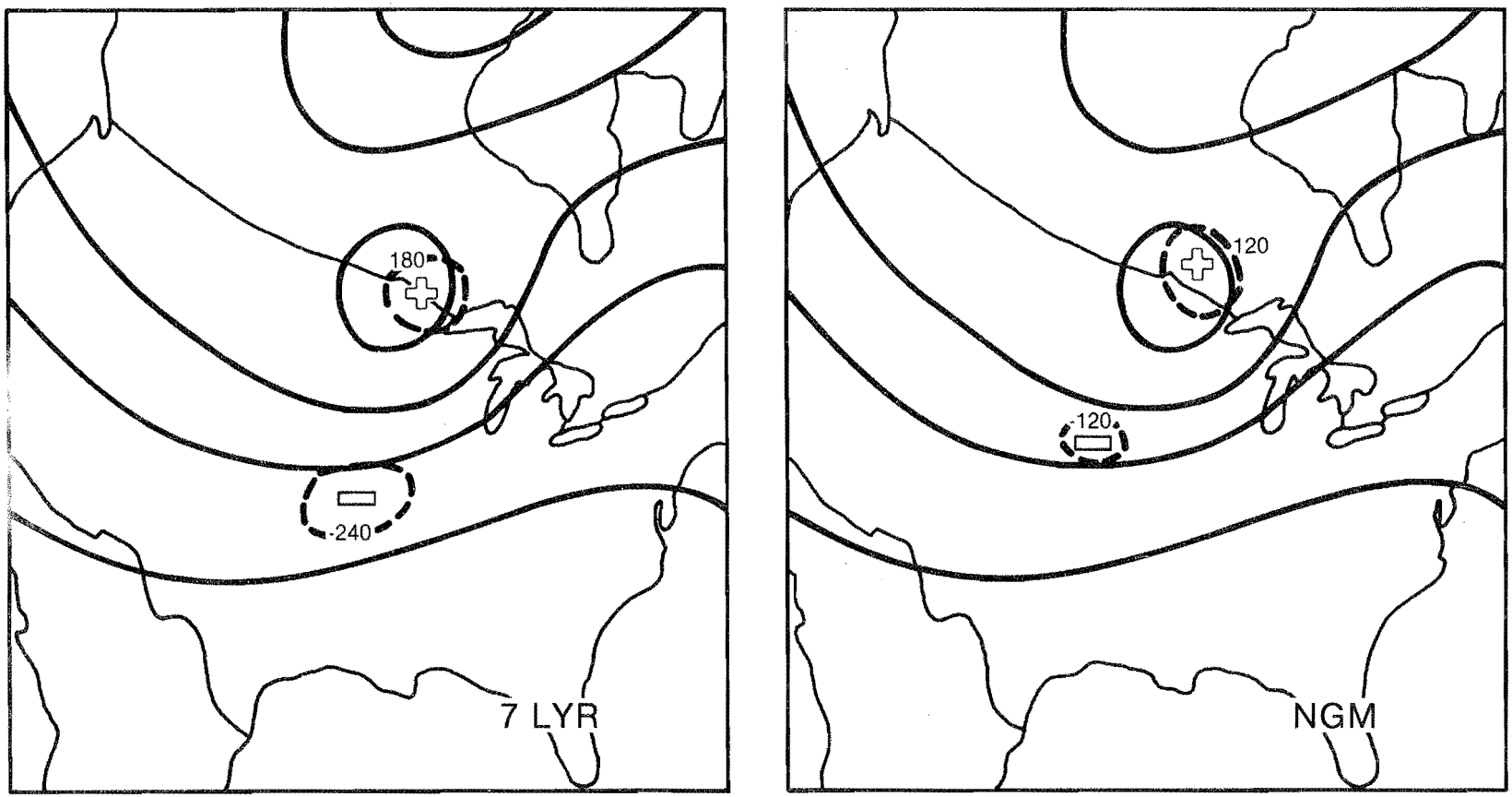

Figure 9.1.--48-hr verifying 500-mb geopotential field (at 180-m intervals, 00Z 21 November 1977, with 48-hr forecast height error centers from the NGM (198 km at 45°N) and the NMC seven-level model (174 km at 45°N).

c. Effects of finer horizontal resolution

The NGM and the seven-level hemispheric model participated in a test of finer horizontal resolution (Phillips 1978), in which 48-hr forecasts from the 19 November 1977 case referred to above and the case of 12Z 9 January 1975 (another locked-in error case) were made with varying horizontal resolutions in each model. For the NGM, 48-hr circulation forecasts with horizontal resolution 99 km at 45° differed only slightly from forecasts made with 198-km resolution. A slight improvement in precipitation forecasts was achieved with the finer resolution, however (figure 9.2). (The seven-level model experienced similar small improvements with increased resolution, but even at 87-km resolution was inferior to the NGM at 198 km in these two locked-in error examples.)

Search for the cause of errors in the NGM forecasts has often uncovered analysis problems. In addition to the six problems discussed at the end of Chapter VI, this search has called attention to the existence of grossly incorrect satellite-measured ocean water temperatures and to the seriousness of the omission of ship air temperatures in the data entering the NMC analysis system (Phillips 1977).

Operational implementation of the NGM does not appear to be a reasonable prospect at this time in spite of the good forecasts it produces on grids B (and C). This is because

(a) The regional model at NMC (the LFM) is now started very early, at 0130Z and 1330Z. This is too soon for all Northern Hemisphere data to reach NMC.

(b) The NGM's typical requirement of 36 min of CPU time per 24-hr forecast in a two-grid format is twice as large as that needed by the LFM. (The NGM requires less I/O time than the LFM but this is not a major factor.)

Difficulty (a) could of course be circumvented by using the previous 12-hr hemispheric forecast in regions away from North America (i.e., in grid A) in place of an updated analysis, much as the LFM depends for its lateral boundary conditions on an earlier hemispheric forecast. Unfortunately, however, the double CPU time factor is a major obstacle in the current operational schedule at NMC. Computational speed-up devices such as pressure-gradient averaging (Brown and Campana 1978), semi-implicit time integration (Robert et al. 1972), and split-explicit integration (Gadd 1978), all require a fundamentally different finite-difference structure than that of the NGM, and therefore cannot be used to reduce its CPU time.

The NGM will therefore in the immediate future be primarily an experimental model, with operational use restricted to the possibility of an "on-call" model for special weather situations.

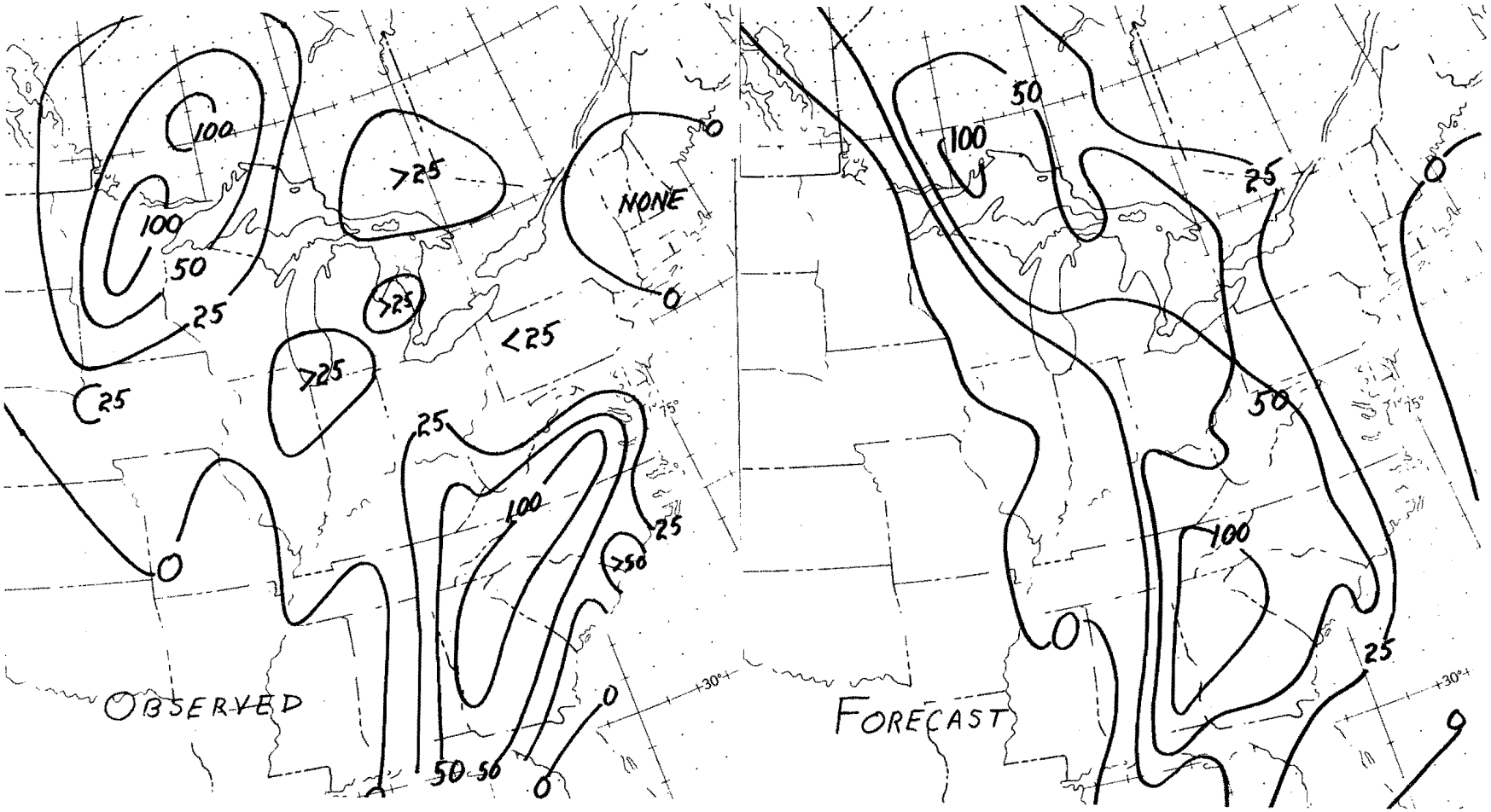

Figure 9.2.--12-hr precipitation 00-12Z 11 January 1975; observed, and from the last 12 hr of a 48-hr NGM forecast (10 levels, 99 km at 45°). Units in 0.01 inches.

REFERENCES

Arakawa, A., and Y. Mintz, 1974: "The UCLA Atmospheric General Circulation Model," Department of Meteorology, UCLA, Los Angeles, Calif. (see Chapters II and III).

Baer, F., 1977: "Adjustment of Initial Conditions Required to Suppress Gravity Oscillations in Non-linear Flows," Beitraege zur Physik der Atmosphaere, 50, 350-366.

Brown, H., and D. Olson, 1978: "Performance of NMC in Forecasting a Record-breaking Winter Storm, 6-7 February 1978," Bulletin of the American Meteorological Society, 59, 562-575.

Brown, J., 1974: "On Vertical Differencing in the σ-system," NMC Office Note 92. (Available from the National Meteorological Center, World Weather Building, Washington, D.C. 20233.)

Brown, J., and K. Campana, 1978: "An Economical Time-differencing System for Numerical Weather Prediction," Monthly Weather Review, 106, 1125-1136.

Campana, K., 1977: "Real Data Experimentation with Higher Order Finite Differencing in the Semi-implicit Version of the Shuman-Hovermale Model," NMC Office Note 163. (Available from the National Meteorological Center, World Weather Building, Washington, D.C. 20233.)

Cressman, G., 1960: "Improved Terrain Effects in Barotropic Forecasts," Monthly Weather Review, 88, 327-342.

Daley, R., 1978: "The Application of Non-linear Normal Mode Initialization to an Operational Forecast Model," Atmosphere, 16, (to appear).

Eliassen, A., 1956: "A Procedure for Numerical Integration of the Primitive Equations of the Two-parameter Model of the Atmosphere," Science Report 4, Department of Meteorology, University of California at Los Angeles, Los Angeles, Calif., 53 pp.

Gadd, A., 1978: "A Split Explicit Integration Scheme for Numerical Weather Prediction," Quarterly Journal of the Royal Meteorological Society, 104, 569-582.

Gerrity, J., 1977: "The LFM Model--1976: A Documentation," NOAA Technical Memorandum NWS NMC-60. (Available from the National Meteorological Center, World Weather Building, Washington, D.C. 20233.)

Kuo, H. L., 1965: "On Formation and Intensification of Tropical Cyclones Through Latent Heat Release by Cumulus Convection," Journal of the Atmospheric Sciences, 22, 40-63.

Lax, P., and B. Wendroff, 1964: "Difference Schemes for Hyperbolic Equations with High Order of Accuracy," Communications on Pure and Applied Mathematics, 381-398.

Machenhauer, B., 1977: "On the Dynamics of Gravity Oscillations in a Shallow Water Model, with Application to Normal Mode Initialization," Contributions to Atmospheric Physics (University of Copenhagen), 50, 253-271.

Miyakoda, K., 1973: "Cumulative Results of Testing a Meteorological-Mathematical Model: The Description of the Model," Proceedings of the Royal Irish Academy, 73(A), No. 9, pp. 99-130.

Ooyama, K., 1969: "Numerical Simulation of the Life Cycle of Tropical Storms," Journal of the Atmospheric Sciences, 26, 3-40.

Phillips, N., 1962: "Numerical Integration of the Hydrostatic System of Equations with a Modified Version of the Eliassen Finite-difference Grid." Proceedings of the International Symposium on Numerical Weather Prediction, Tokyo, November 1960, Meteorological Society of Japan, pp. 109-120.

Phillips, N., 1974: "Application of Arakawa's Energy-conserving Scheme to Operational Numerical Weather Prediction," NMC Office Note 104. (Available from the National Meteorological Center, World Weather Building, Washington, D.C. 20233.)

Phillips, N., 1977: "Data and Analysis Errors on 9 January 1977," NMC Office Note 160. (Available from the National Meteorological Center, World Weather Building, Washington, D.C. 20233.)

Phillips, N., 1978: "A Test of Finer Resolution," NMC Office Note 171. (Available from the National Meteorological Center, World Weather Building, Washington, D.C. 20233.)

Phillips, N., and J. Shukla, 1973: "On the Strategy of Combining Coarse and Fine Grid Meshes in Numerical Weather Prediction," Journal of Applied Meteorology, 12, 763-770.

Robert, A., J. Henderson, and C. Turnbull, 1972: "An Implicit Time Integration Scheme for Baroclinic Models of the Atmosphere," Monthly Weather Review, 100, 329-335.

Rossby, C. -G., 1932: Thermodynamics Applied to Air Mass Analysis," Papers in Physical Oceanography and Meteorology, Woods Hole, vol. 1, No. 3.

Shapiro, R., 1975: "Linear Filtering," Mathematical Computations, 29, 1094-1097.

Shuman, F., 1962: "Numerical Experiments with the Primitive Equations," Proceedings of the International Symposium on Numerical Weather Prediction, Tokyo, Japan, November 1960. Meteorological Society of Japan, pp. 85-107, (see page 98).

Shuman, F., and J. Hovermale, 1968: "An Operational Six-layer Primitive Equation Model," Journal of Applied Meteorology, 7, 525-547.

Stackpole, J., 1978a: "The NMC 9-layer Global Primitive Equation Model on a Latitude-longitude Grid," NMC Office Note 178. (Available from the National Meteorological Center, World Weather Building, Washington, D.C. 20233.)

Stackpole, J., et al., 1978b: "How to Pick a New Forecast Model: The Selection of the 7L PE for NMC Operations," NMC Office Note 191.. (Available from the National Meteorological Center, World Weather Building, Washington, D.C. 20233.)

Sundqvist, H., 1976: "On Vertical Interpolation and Truncation in Connection with Use of Sigma System Models." Atmosphere, 14, 37-52.

APPENDIX A

VERTICAL FUNCTIONS AND THE HYDROSTATIC EQUATION

In describing the finite-difference equations, the Fortran symbols used in the NGM code will be used when possible. Date records transferred between disk and core during the forecast operation consist of units containing all data that have a common j subscript on one grid. Only full time step data are transferred in this way, since the forecast codes are written to forecast the half time step and full time step variables for one j-value before proceeding to the next. This is done in sequence H'_j, u'_j, v'_j, θ'_j, q'_j, followed by the new time step values of H_j, Hu_{j-1}, Hv_j, H_j--a sequence that minimizes internal storage requirements set mostly by the horizontal averages involved in the turbulent vertical flux terms. This sequential marching in j is not recognized, however, in the finite-difference equations as they are recorded in Appendixes A-H.

Certain fixed functions of k only are used by all grids:

$$DEL_k = \Delta\sigma_k \tag{A.1}$$

$ES_k (= 1-\hat{\sigma}_k)$:

$$ES_1 = 1,$$

$$ES_{k+1} = ES_k - DEL_k \quad (k = 1,\ldots,K-1),$$

$$ES_{K+1} = 0. \tag{A.2}$$

(i.e., ES is the conventional "σ" = p/H at the interfaces).

$$DELK_k = \Delta t/(4\Delta \cdot DEL_k) \tag{A.3}$$

$$DELKH_k = 0.5\ DELK_k \tag{A.4}$$

$$DEL1_k = \Delta t/DEL_k \tag{A.5}$$

$$DEL2_k = 0.5\ DEL1_k \tag{A.6}$$

The following three functions are used in computing $\pi = p^\kappa$ in the layers (times 0.5), pressure in the layers, and a weighting function for the layer 1 hydrostatic relation. (Recall that H is the surface pressure.)

$$PR_k (= 0.5\ \pi_k/H^\kappa) = \frac{ES_k^{1+\kappa} - ES_{k+1}^{1+\kappa}}{2(1+\kappa)DEL_k} \tag{A.7}$$

$$\mathrm{PRESS}_k (= p_k/H) = (2\ \mathrm{PR}_k)^{1/\kappa} \tag{A.8}$$

$$\begin{aligned} \mathrm{TW}_k &= [\kappa\ \pi_k \Delta\sigma_k - \tfrac{1}{2}(1-\hat{\sigma}_k)(\pi_{k-1} - \pi_k) - \tfrac{1}{2}(1-\hat{\sigma}_{k+1})(\pi_k - \pi_{k+1})]/H^{\kappa} \\ &= 2\kappa \mathrm{PR}_k \mathrm{DEL}_k - \mathrm{ES}_k(\mathrm{PR}_{k-1} - \mathrm{PR}_k) - \mathrm{ES}_{k+1}(\mathrm{PR}_k - \mathrm{PR}_{k+1}). \end{aligned} \tag{A.9}$$

In this last formula, PR for k-1 = 0 is by definition equal to PR at k = 1. The special definition above of the layer pressure amounts to choosing

$$p_k = \left(\frac{\hat{p}_k^{\,1+\kappa} - \hat{p}_{k+1}^{\,1+\kappa}}{(1+\kappa)(\hat{p}_k - \hat{p}_{k+1})} \right)^{1/\kappa} \tag{A.10}$$

and is the formula suggested by Brown (1974) and Phillips (1974). It has the virtue of assigning the exact dry enthalpy to a sigma layer if that layer has an adiabatic stratification.[1]

In the code, geopotential ϕ is computed (and stored) for convenience, as a "temperature" ψ:

$$\psi \equiv \phi/c_p, \tag{A.11}$$

including the surface geopotential. Both steps in the Lax-Wendroff double time step (see Chapter II and figure 2.1) compute the geopotential field ψ (or ψ') from H, θ (or H', θ') in the same way. After H^{κ} is computed from H, 0.5 π_k is computed (for a column of fixed i,j) by

$$\mathrm{PI}_k (= \tfrac{1}{2}\ \pi_k) = H^{\kappa}\ \mathrm{PR}_k. \tag{A.12}$$

ψ for layer 1 is computed from

$$\mathrm{PSI}_1 = \mathrm{SPSI} + H^{\kappa} \sum_{k=1}^{K} \mathrm{TW}_k\ \theta_k \tag{A.13}$$

---

[1]Contrary to some early hopes raised in Phillips (1974), this definition has not by itself reduced the vertical truncation error in the sigma coordinate pressure force over steep orographic slopes.

where SPSI = $\psi_g = \phi_g/c_p$ is the ground "geopotential." (When this equation is used to get ψ' from H' and θ', SPSI at the center of the grid square of figure 2.1 is evaluated as one-quarter of the SPSI values summed at the four surrounding H points.) Then, for layers $k = 2,\ldots,K$:

$$PSI_k = PSI_{k-1} + (PI_{k-1} - PI_k)\cdot(\theta_k + \theta_{k-1}). \qquad (A.14)$$

Equation (A.14) is an obvious centered approximation to the continuous hydrostatic eq (2.1). Equation (A.13), however, is a special relation derived by Arakawa (Arakawa and Mintz 1974). It is discussed in Appendix B.

APPENDIX B

THE HORIZONTAL PRESSURE FORCE

Throughout the NGM code, the scale factor $m = 2(1 + \sin\Theta)^{-1}$ defined in eq (2.7) is computed directly only at the H points in figure 2.1.

$$m_{ij}(\text{H point}) = 1 + \left(\frac{\Delta}{2a}\right)^2 [(i-i_p)^2 + (j-j_p)^2].$$

When m is needed at any of the three other points shown on figure 2.1, it is obtained by averaging the H point values. The error is at most $0.5(\Delta/2a)^2 \sim (2 \cdot NH^2)^{-1} \sim 1/1700$ on grid A, and 1/4 or 1/16 of this on grids B or C.

The x-component of the pressure force in the half time step of eq (2.12) is evaluated at the Hv point of figure 2.1. With

$$GUPP_{ij} = \left(\frac{c_p \Delta t}{4\Delta}\right)(m_{ij} + m_{i+ij}), \tag{B.1}$$

the computation proceeds as

$$-\frac{\Delta t m}{2}\left(\frac{\partial \phi}{\partial x} + c_p\, \theta \frac{\partial \pi}{\partial x}\right) = GUPP_{ij}[PSI_i - PSI_{i+1} + (\theta_{i+1} + \theta_i)(PI_i - PI_{i+1})]_{jk}. \tag{B.2}$$

At the full time step, the x-component of the pressure force in eq (2.17), multiplied by Δt, can be rewritten as

$$-\Delta t m\, H\left(\frac{\partial \phi}{\partial x} + c_p\, \theta \frac{\partial \pi}{\partial x}\right) = -\Delta t\, m \left[\frac{\partial H \phi}{\partial x} - (\phi - R\pi\phi)\frac{\partial H}{\partial x}\right], \tag{B.3}$$

This is evaluated at the Hu position of figure 2.1 using H', θ', and ψ' at i,j and i-1,j, with the following sequence.

$$GUP_{ij} = \left(\frac{c_p \Delta t}{2\Delta}\right)(m_{ij} + m_{ij+1}) \tag{B.4}$$

$$DELXH_{ij} = H'_{ij} - H'_{i-ij} \tag{B.5}$$

$$HPSI_{ijk} = H'_{ij}\ PSI'_{ijk} \tag{B.6}$$

$$S_{ijk} = 0.5\ PSI'_{ijk} - \kappa\ PI'_{ijk}\ \theta'_{ijk} \tag{B.7}$$

$$\text{eq (B.3)} = GUP_{ij}[HPSI_{i-1} - HPSI_i + (S_i + S_{i-1})DELXH_i]_{jk} \tag{B.8}$$

The y-component of the pressure force in eq (2.13) and (2.18) is computed in a completely analogous way, with due attention to the staggered variable locations in figure 2.1.

The special hydrostatic relation eq (A.13) for layer 1 was derived by Arakawa so that the finite-difference forecast system will satisfy an analog to the following vertical integral of the continuous pressure force:

$$-\int_0^H \nabla\phi \, dp = -\nabla \int_0^H \phi \, dp + \phi_g \nabla H, \tag{B.9}$$

the last term of which represents the form drag over variable terrain. This may be demonstrated in the present sigma system by evaluating the sum of S in eq (B.8):

$$2\sum_{k=1}^{K} S_k \Delta\sigma_k = \sum_{k=1}^{K} (\psi_k - \kappa \, \pi_k \, \theta_k)\Delta\sigma_k. \tag{B.10}$$

If we define $\hat{s}_k = 1 - \hat{\sigma}_k$, so that $\Delta\sigma_k = \hat{s}_k - \hat{s}_{k+1}$, the ψ sum in eq (B.10) can be written as

$$\sum_{k=1}^{K} \psi_k \, \Delta\sigma_k = \psi_1 + \sum_{k=2}^{K} \hat{s}_k(\psi_k - \psi_{k-1}). \tag{B.11}$$

Use of eq (A.13) and (A.14) allows this to be rewritten

$$\sum_{k=1}^{K} \psi_k \Delta\sigma_k = \psi_g + \kappa \sum_{k=1}^{K} \pi_k \theta_k \Delta\sigma_k - \tfrac{1}{2}\left(\sum_{k=1}^{K} (\alpha_k + \alpha_{k+1})\theta_k - \sum_{k=2}^{K} \alpha_k (\theta_k + \theta_{k-1}) \right) \tag{B.12}$$

where, for brevity,

$$\alpha_k = \hat{s}_k(\pi_{k-1} - \pi_k).$$

α_k vanishes at $k = K+1$ (where $\hat{s}_k = 0$) and $k = 1$ (where $\pi_0 = \pi_1$ by definition). All $\alpha\theta$ terms now cancel in eq (B.12), so that

$$2\sum_{k=1}^{K} S_k \Delta\sigma_k = \psi_g$$

and the DELXH_i contribution to eq (B.8) yields directly the $\phi_g \nabla H$ term of the momentum integral eq (B.9).

APPENDIX C

THE CONTINUITY EQUATION

It is convenient to define

$$\hat{W}_k = \Delta\ H \left(\frac{d\hat{\sigma}}{dt}\right)_k \tag{C.1}$$

as a modified vertical sigma velocity, valid at the interfaces. The boundary conditions are

$$\hat{W}_k = 0 \text{ at } k=1 \text{ and } K+1. \tag{C.2}$$

In the half time step, $\hat{W}_k$ and $\partial H/\partial t$ are computed at the center of the grid square in figure 2.1. After a preliminary computation of

$$GIU_{ij} = (m_j + m_{j+1})^{-1}_i, \tag{C.3}$$

$$GIV_{ij} = (m_i + m_{i+1})^{-1}_j \tag{C.4}$$

$$GMC2_{ij} = \tfrac{1}{8}[m_{ij} + m_{i+1j} + m_{ij+1} + m_{i+1j+1}]^2, \tag{C.5}$$

the x- and y-mass fluxes

$$FX_{ijk} \left(= \tfrac{1}{2}\frac{Hu}{m}\right) = GIU_{ij} \cdot HU_{ijk} \tag{C.6}$$

$$FY_{ijk} \left(= \tfrac{1}{2}\frac{Hv}{m}\right) = GIV_{ij} \cdot HV_{ijk} \tag{C.7}$$

are first computed. The horizontal mass convergence is then calculated in the form

$$CONV_{ijk}\left(= - m^2\Delta\ \Delta\sigma_k\left(\frac{\partial}{\partial x}\left(\frac{Hu}{m}\right) + \frac{\partial}{\partial y}\left(\frac{Hv}{m}\right)\right)\right)$$

$$= GMC2_{ij}\ DEL_k(FX_{ij} - FX_{i+1j} + FY_{ij} - FY_{ij+1})_k, \tag{C.8}$$

which is a centered expression valid in the center of the grid square of figure 2.1.

The vertical sum of eq (C.8) now gives the analog to eq (2.9):

$$DH'_{ij}\left(=\Delta\frac{\partial H}{\partial t}\right) = \sum_{k=1}^{K} CONV_{ijk}. \tag{C.9}$$

Following this, H′ at the center of the grid square is given by

$$H'_{ij} = \tfrac{1}{4}[H_{ij} + H_{i+1j} + H_{ij+1} + H_{i+ij+1}] + \left(\frac{\Delta t}{2\Delta}\right)DH'_{ij}. \tag{C.10}$$

The final part of the half time step is to compute the W field at the interfaces:

$$k = 1: \quad \hat{W}_{ij1} = 0, \tag{C.11}$$

$$k = 2,\ldots,K: \quad \hat{W}_{ijk} = W_{ijk-1} - DEL_{k-1} \cdot DH'_{ij} + CONV_{ijk-1}, \tag{C.12}$$

$$k = K+1: \quad \hat{W}_{ijK+1} = 0. \tag{C.13}$$

For the full time step, $\partial H/\partial t$ and $\hat{W}'$ are evaluated at the H points of figure 2.1 by the following scheme. First

$$HDVMX_{ij} = (H'_{ij} + H'_{ij-1})/(m_{ij} + m_{i+ij}), \tag{C.14}$$

and

$$HDVMY_{ij} = (H'_{ij} + H'_{i-1j})/(m_{ij} + m_{ij+1}) \tag{C.15}$$

are computed as approximations to H/m at the location of the u′ and v′ points of figure 2.1. Mass fluxes in the x- and y-directions at those points are then given:

$$FHX\left(=\frac{Hu}{m}\right) = HDVMX_{ij}\ u'_{ijk} \tag{C.16}$$

$$FHY\left(=\frac{Hv}{m}\right) = HDVMY_{ij}\ v'_{ijk}. \tag{C.17}$$

The CONV expression in eq (C.8) in this step is evaluated at he H point of figure 2.1:

$$CONV'_{ijk} = m_{ij}^2\ DEL_k(FHX_{i-1j} - FHX_{ij} + FHY_{ij-1} - FHY_{ij})_k. \tag{C.18}$$

DH and W′ are now computed just as in eq (C.9) and (C.12), but the full time step equivalent of eq (C.10) is

$$H_{ij}(t+\Delta t) = H_{ij}(t) + \left(\frac{\Delta t}{\Delta}\right)DH_{ij}\ . \tag{C.19}$$

APPENDIX D

THE CORIOLIS FORCE

The half and full time step Coriolis coefficient f´ and Hf´ in eq (2.12), (2.13), (2.16), (2.17), and (2.18) are evaluated first at the H points of figure 2.1 in the sequence

$$GCORH_{ij} \left(= \frac{\Delta t}{2} 2\Omega H \sin\theta\right) = (2\Omega\Delta t)\left(\frac{1}{m_{ij}} - 0.5\right)H_{ij} \tag{D.1}$$

$$GCORU_j \ (= y\Delta t/8a^2) = \left(\frac{\Delta\ \Delta t}{8a^2}\right)(j - j_p) \tag{D.2}$$

$$GCORV_i \ (= - x\Delta t/8a^2) = \left(- \frac{\Delta\ \Delta t}{8a^2}\right)(i - i_p) \tag{D.3}$$

$$COR_{ijk} \left(= \frac{H\Delta t}{2} f'\right) = GCORH_{ij} + \left[(HU)_{j-1} + (HU)_j\right]_{ik} \cdot GCORU_j$$

$$+ \left[(HV)_{i-1} + HV_i\right]_{jk} \cdot GCORV_i \cdot \tag{D.4}$$

This last expression is used in both the half and full time step.

For the half time step, $\Delta t/2$ times the f´v and -f´u in eq (2.12) and (2.13) are then given, at the u´ and v´ points of figure 2.1, respectively, by

$$(COR_i + COR_{i+1})_{jk} \, v_{ijk}/(H_{ij} + H_{i+1j}) \tag{D.5}$$

and

$$- (COR_j + COR_{j+1})_{ik} \, u_{ijk}/(H_{ij} + H_{ij+1}) \tag{D.6}$$

where v and u are obtained from HV and HU: $2(HV)_{ijk}/(H_i + H_{i+1})_j$ and $2(HU)_{ijk}/(H_j + H_{j+1})_i$.

For the full time step, $\Delta t Hf´v$ and $-\Delta t Hf´u$ in eq (2.17) and (2.18) are obtained more simply:

$$\Delta t \ Hf´v = (COR_j + COR_{j+1})_{ik} \, v´_{ijk}, \tag{D.7}$$

$$- \Delta t \ Hf´u = - (COR_i + COR_{i+1})_{jk} \, u´_{ijk}, \tag{D.8}$$

valid at the Hu and Hv points, respectively.

Alternate forms for these Coriolis terms are possible, but the above seem to be satisfactory.

APPENDIX E

THE ADVECTION OPERATOR FOR THE HALF TIME STEP

The operator A defined in eq (2.11) and used in eq (2.12)-(2.15) is combined with the $\Delta t/2$ time extrapolation to give an advected value of h denoted by $\tilde{h}$:

$$\tilde{h} = \bar{h} - \frac{\Delta t}{2}\left(m\left(u\frac{\partial h}{\partial x} + v\frac{\partial h}{\partial y}\right) + \dot{\sigma}\frac{\partial h}{\partial \sigma}\right). \tag{E.1}$$

The half time step forecast h′ will equal $\tilde{h}$ plus $\Delta t/2$ times the remaining terms on the r.h.s. of eq (2.12)-(2.15):

$$h' = \tilde{h} + \frac{\Delta t}{2}\frac{dh}{dt}\ . \tag{E.2}$$

The evaluation of $\tilde{h}$ is carried out as follows: figure E.1 indicates the relative location of one of the full time step variables h

$$h = (u,\ v,\ \theta,\ \text{or } q) \tag{E.3}$$

at the corners of its "own" grid square, and the location of $\tilde{h}$ and h′ in the center of the square. (The full time step u, v, θ, and q are obtained from Hu, Hv, and Hq by division with an appropriate value of H.)

Let A and B denote the following combinations of h at time t in layer k for the j-row being forecast [j and k are now implicit until eq (E.13).]

$$A_i = \tfrac{1}{4}(h_c + h_a)_i\ , \tag{E.4}$$

$$B_i = \tfrac{1}{4}(h_c - h_a)_i\ . \tag{E.5}$$

Then $\bar{h}$, at point o in layer k at time t is given by

$$\bar{h} = A_i + A_{i+1}\ . \tag{E.6}$$

Now let

$$XI_i \sim \frac{\Delta t}{\Delta} m\ u, \tag{E.7}$$

$$ETA_i \sim \frac{\Delta t}{\Delta} m\ v, \tag{E.8}$$

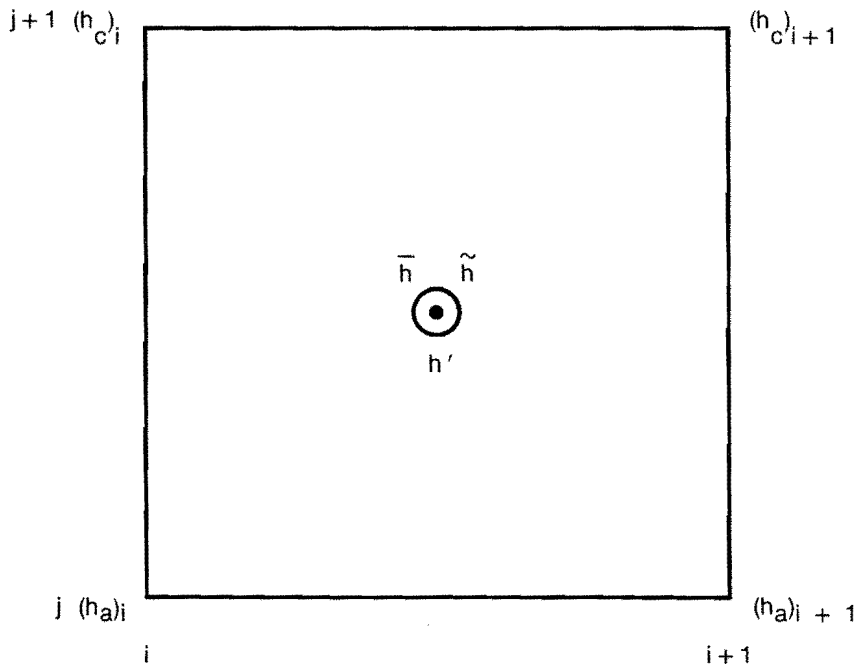

Figure E.1.--Relative location, in a square region of area Δ^2 of the h_a and h_c full time step values, of a variable h that is to be forecast at $t + \frac{1}{2}\Delta t$ at point 0 in the half time step advection operation.

represent appropriate estimates of the horizontal particle displacement (in units of the grid increment Δ) at layer k at point o, that would take place in a time Δt. (They are constructed as shown below, from the values of Hu and Hv at time t in the vicinity of o.) The horizontal advection portion of eq (E.1) is evaluated as

$$-\frac{\Delta t}{2} m\left(u\frac{\partial h}{\partial x} + v\frac{\partial h}{\partial y}\right) = XI_i (A_i - A_{i+1}) - ETA_i (B_i + B_{i+1}) . \qquad (E.9)$$

The vertical advection term in $-(\Delta t/2)\dot{\sigma}\ \partial h/\partial\sigma$ is evaluated in the following way. First let

$$\hat{ZETA}_k \sim \Delta\left(\frac{\hat{d\sigma}}{dt}\right)_k \qquad (E.10)$$

be a value appropriate to point o at interface k. Then

$$-\left(\frac{\Delta t}{2\Delta}\right)\frac{ZETA_k(\bar{h}_k - \bar{h}_{k-1})}{(\Delta\sigma_k + \Delta\sigma_{k-1})} \qquad (E.11)$$

is a valid approximation to the desired term at interface k. At k = 1 and K+1, eq (E.11) vanishes, and the appropriate layer value of $-(\Delta t/2)\dot{\sigma}\ \partial h/\partial\sigma$ is

$$\tfrac{1}{2}[(E.11)_k + (E.11)_{k+1}], \quad k = 1,\ldots,K. \qquad (E.12)$$

The displacements XI, ETA that are appropriate to each forecast variable in the above scheme are computed at each layer from basic displacements XDIS and YDIS valid at the Hu and Hv locations of figure 2.1.

$$XDIS_{ijk} = (m_j + m_{j+1})_i \frac{\Delta t\ u_{ijk}}{4\Delta} \qquad (E.13)$$

$$YDIS_{ijk} = (m_i + m_{i+1})_j \frac{\Delta t\ v_{ijk}}{4\Delta} \qquad (E.14)$$

where

$$u_{ijk} = 2(HU)_{ijk}/(H_{j+1} + H_j)_i \qquad (E.15)$$

$$v_{ijk} = 2(HV)_{ijk}/(H_i + H_{i+1})_j \qquad (E.16)$$

The interface parameter $\hat{ZETA}$ is computed from the $\hat{W}$ of eq (C.1) and (C.12) by means of

$$\hat{ZDIS}_{ijk} = \frac{4\hat{W}_{ijk}}{(H_{ij} + H_{i+1j} + H_{i+1j+1})} . \qquad (E.17)$$

It is therefore valid at the center of the grid square of figure 2.1.

Table E.1 tabulates, for each forecast variable u', v', θ', and q', the horizontal location of the h_c and h_a points used in eq (E.4) and (E.5) to get the A_i and B_i used for forecasting u', v', θ', and q'. The table also shows the way in which values of XI, ETA, and ZETA at the forecast point are computed from the basic quantities $XDIS_{ij}$, $YDIS_{ij}$, and $ZDIS_{ij}$.

Table E.1.--Horizontal identification with respect to figure 2.1 of the variables h_c and h_a of figure E.1, and the definition of XI, ETA, ZETA in terms of the basic displacements X = XDIS, Y = YDIS, and Z = ZDIS.

	Forecast variable		
	u'_{ij}	v'_{ij}	θ'_{ij} (and q'_{ij})
h_c	u_{ij}	v_{i-1j+1}	$\theta_{ij+1}(q_{ij+1})$
h_a	u_{ij-1}	v_{i-1j}	$\theta_{ij}(q_{ij})$
XI	$0.5(X_{ij}+X_{i+1j}+X_{ij-1}+X_{i+1j-1})$	$2X_{ij}$	$X_{ij}+X_{i+1j}$
ETA	$2Y_{ij}$	$0.5(Y_{i-1j}+Y_{ij}+Y_{i-1j+1}+Y_{ij+1})$	$Y_{ij}+Y_{ij+1}$
ZETA	$Z_{ij}+Z_{ij-1}$	$Z_{ij}+Z_{i-1j}$	$2Z_{ij}$

APPENDIX F

THE FLUX OPERATOR FOR THE FULL TIME STEP

The operation $-\Delta t$ times the B(Hh) appearing in eq (2.17)-(2.20) is evaluated using the half time step variables H', u', v', θ', and q'. The two mass fluxes

$$FHX_{ijk} \sim \frac{H'u'}{m} \tag{F.1}$$

$$FHY_{ijk} \sim \frac{H'v'}{m} \tag{F.2}$$

previously used in the full time step continuity equation (C.18) are used again, together with the full time step vertical velocity W'. The latter is valid at the H point of figure 2.1, while eq (F.1) and (F.2) are valid at the u' and v' points in that diagram.

For each variable, h, horizontal fluxes equivalent to 2h(Hu/m) and 2h(Hv/m) are computed for each layer k:

$$FXU_{ij} = (u'_j\ FHX_j + u'_{j+1}\ FHX_{j+1})_i, \tag{F.3}$$

$$FYU_{ij} = 0.5(u'_i + u'_{i-1})_j (FHY_{j-1} + FHY_j)_i, \tag{F.4}$$

$$FXV_{ij} = 0.5(v'_j + v'_{j-1})_i (FHX_i + FHX_{i-1})_j, \tag{F.5}$$

$$FYV_{ij} = (v'_i FHY_i + v'_{i+1}\ FHY_{i+1})_j, \tag{F.6}$$

$$FXQ_{ij} = (q'_j + q'_{j-1})_i\ FHX_{ij}, \tag{F.7}$$

$$FYQ_{ij} = (q'_i + q'_{i-1})_j\ FHY_{ij}. \tag{F.8}$$

(Hθ is treated completely parallel to Hq and therefore need not be recorded here.) These six flux measures are valid, respectively, at the H', H, H, H', Hv, and Hu points of figure 2.1.

A vertical flux ($\sim 2\Delta H\dot{\theta}h$) is defined for all variables at the interfaces, at the H points of figure 2.1. This requires averaging of h' in layers k and k-1.

$$F\hat{Z}U_{ijk} = \hat{W}'_{ijk}\ \tfrac{1}{2}[u'_{ik} + u'_{i-1k} + u'_{ik-1} + u'_{i-1k-1}]_j, \tag{F.9}$$

$$F\hat{Z}V_{ijk} = \hat{W}'\ \tfrac{1}{2}[v'_{jk} + v'_{j-1k} + v'_{jk-1} + v'_{j-1k-1}]_i, \tag{F.10}$$

$$F\hat{Z}Q_{ijk} = \hat{W}'_{ijk}[q'_{ijk} + q'_{i-1jk} + q'_{ij-1k} + q'_{i-1j-1k} + q'_{ijk-1} + q'_{i-1jk-1} + q'_{ij-1k-1} + q'_{i-1j-1k-1}]. \tag{F.11}$$

The full time step advection change $\delta(Hh)$ in the variable Hh from t to $t+\Delta t$ is given by $-\Delta t B(Hh)$. In terms of the above fluxes, this is

$$\delta(HU)_{ijk} = \left(\frac{\Delta t}{8\Delta}\right)(m_j + m_{j+1})_i^2 [FXU_{i-1} - FXU_i)_j + (FYU_j - FYU_{j+1})_i]_k$$
$$+ DELK_k[(FZU_j + FZU_{j+1})_k - (FZU_j + FZU_{j+1})_{k+1}]_i, \qquad (F.12)$$

$$\delta(HV)_{ijk} = \left(\frac{\Delta t}{8\Delta}\right)(m_i + m_{i+1})_j^2 [FXV_i - FXV_{i+1})_j + (FYV_{j-1} - FYV_j)_i]_k$$
$$+ DELK_k[(FZV_i + FZV_{i+1})_k - (FZV_i + FZV_{i+1})_{k+1}]_i, \qquad (F.13)$$

$$\delta(HQ)_{ijk} = \left(\frac{\Delta t}{2\Delta}\right)m_{ij}^2[(FXQ_{i-1} - FXQ_i)_j + (FYQ_{j-1} - FYQ_j)_i]_k$$
$$+ DELKH_k(FZQ_k - FZQ_{k+1})_{ij}, \qquad (F.14)$$

where $DELK_k$ and $DELH_k$ are defined in eq (A.3) and (A.4).

The above changes (including that for $H\theta$) are added to (Hh) at time step t, together with Δt times the remaining terms on the r.h.s. of eq (2.17)-(2.20) to give (Hh) at time step $t+\Delta t$. [Note, however, that $\delta(HQ)$ can be adjusted in the moist convection process described in Chapter IV.]

APPENDIX G

NUMERICAL EVALUATION OF THE TURBULENT VERTICAL FLUXES

The exchange coefficients described in Chapter III are evaluated only at the H points of figure 2.1 and from the full time step variables.

For $\hat{F}_1$ in eq (3.2), $|\vec{v}_{an}|$ is computed by the formula

$$\frac{ANEM}{2H_{ij}}[(HU_j + HU_{j-1})_i^2 + (HV_i + HV_{i-1})_j^2]_{k=1} \tag{G.1}$$

where, as mentioned in Chapter III, a value of 0.8 has proved satisfactory for ANEM.

For the interior $\hat{F}_k$ defined in eq (3.5), we first express the Richardson number at interface k as

$$\begin{aligned} Ri &= (gd\ell n\theta/dz)/(d\vec{v}/dz)^2 \\ &= -c_p(d\theta/d\pi)/(dv/d\pi)^2 \\ &\simeq \frac{c_p(\theta_k - \theta_{k-1})(\pi_{k-1} - \pi_k)}{(\vec{v}_k - \vec{v}_{k-1})^2} \end{aligned} \tag{G.2}$$

by using the hydrostatic relation $gdz = -c_p\theta d\pi$. The π difference in eq (G.2) is expressed as $2H^K(PR_{k-1} - PR_k)$, according to eq (A.7). The denominator is evaluated as

$$1 + (USHR^2 + VSHR^2) \tag{G.3}$$

where USHR and VSHR are constructed from the full time step U and V values by horizontal averaging

$$USHR = \tfrac{1}{2}[(U_j + U_{j-1})_k - (U_j + U_{j-1})_{k-1}]_i, \tag{G.4}$$

$$VSHR = \tfrac{1}{2}[(V_i + V_{i-1})_k - (V_i + V_{i-1})_{k-1}]_j, \tag{G.5}$$

(The small added term 1 in eq (G.3) is used to avoid the possibility of computational "overflow" when the shear happens to be extremely small.)

The frictional effects in the x and y directions are expressed as Δt times the frictional accelerations:

$$FRX_{ijk} = \Delta t \frac{\partial(Fu)}{\partial\sigma} \tag{G.6}$$

$$FRY_{ijk} = \Delta t \frac{\partial(Fv)}{\partial\sigma} . \tag{G.7}$$

They are evaluated only at the beginning of the time step, FRX at the Hu point of figure 2.1, and FRY at the Hv point. This requires horizontal averaging of the exchange coefficients,

$$\hat{F}_{ijk} \text{ (for FRX)} = \tfrac{1}{2}(\hat{F}_j + \hat{F}_{j+1})_{ik}, \tag{G.8}$$

$$\hat{F}_{ijk} \text{ (for FRY)} = \tfrac{1}{2}(\hat{F}_i + \hat{F}_{i+1})_{jk}. \tag{G.9}$$

With these definitions of F understood, vertical fluxes are computed at the surface and at the higher interfaces k=2,...,K according to the scheme

$$\hat{FU}_{ij1} = \hat{F}_1(u_{an})_{ij} \tag{G.10}$$

$$\hat{FU}_{ijk} = \hat{F}_k(U_k - U_{k-1})_{ij} \tag{G.11}$$

$$\hat{FV}_{ij1} = \hat{F}_1(v_{an})_{ij} \tag{G.12}$$

$$\hat{FV}_{ijk} = \hat{F}_k(V_k - V_{k-1})_{ij}. \tag{G.13}$$

They vanish at k = K+1. u_{an} and v_{an} are not only reduced by the factor ANEM from u and v in layer 1, they are rotated by 22.5°, as described in Chapter III. The frictional effects for one time step at the Hu and Hv points are now given by

$$FRX_{ijk} = DELl_k(FU_{k+1} - FU_k)_{ij}, \tag{G.14}$$

$$FRY_{ijk} = DELl_k(FV_{k+1} - FV_k)_{ij}, \tag{G.15}$$

and are valid at the Hu and Hv points, respectively, in figure 2.1.

The turbulent terms in eq (2.14), (2.15), and (2.19), (2.20) are computed at the H points, using the full time step variables. At the ocean surfaces, the surface fluxes are

$$\hat{FT}_1 = \hat{F}_1(\hat{\pi}_1\theta_1 - T_{water}) \tag{G.16}$$

$$\hat{FQ}_1 = \hat{F}_1(q_1 - q_{water}) . \tag{G.17}$$

Over land these are replaced by zero, since they depend on the heat balance of the soil, and this cannot be computed in the absence of radiation fluxes. At higher interfaces (over land and ocean),

$$\hat{FT}_k = \hat{F}_k(\theta_k - \theta_{k-1}), \tag{G.18}$$

$$\hat{FQ}_k = \hat{F}_k(q_k - q_{k-1}). \tag{G.19}$$

Following this, the full time step effects are expressed in the forms

$$HTGDRY_k = \frac{DEL2_k}{(0.5\pi_k)} (\hat{FT}_{k+1} - \hat{FT}_k), \tag{G.20}$$

$$QTRB_k = DEL1_k(\hat{FQ}_{k+1} - \hat{FQ}_k). \tag{G.21}$$

(Recall that $\hat{F}_{K+1} = 0.$)

The four turbulence terms eq (G.14), (G.15), (G.20), and (G.21) represent this effect from time t to t+Δt, and have been computed using the variables at time t. They are used in the prediction equations for the half time step by adding, for each layer k, half their value to the advected variable value described in Appendix E. This requires horizontal averaging. Thus,

$$\frac{1}{8}[FRX_{ij} + FRX_{i+1j} + FRX_{ij-1} + FRX_{i+1j-1}]_k, \tag{G.22}$$

$$\frac{1}{8}[FRY_{ij} + FRY_{i-1j} + FRY_{ij+1} + FRY_{i-1j+1}]_k, \tag{G.23}$$

$$\frac{1}{8}[HTGDRY_{ij} + HTGDRY_{i+1j} + HTGDRY_{ij+1} + HTGDRY_{i+1j+1}]_k, \tag{G.24}$$

and

$$\frac{1}{8}[QTRB_{ij} + QTRB_{i+1j} + QTRB_{ij+1} + QTRB_{i+1j+1}]_k \tag{G.25}$$

are added in the computation of u′, v′, θ′, and q′ at the half time step. For the full time step, horizontal averaging is not needed except for some of the H multipliers: $\frac{1}{2}(H_j + H_{j+1})_i$ FRX_{ij}, $\frac{1}{2}(H_i + H_{i+1})_j$ FRY_{ij}, H_{ij} $HTGDRY_{ij}$, and H_{ij} $QTRB_{ij}$ are simply added in the computation of Hu, Hv, Hθ, and Hq at t+Δt.

APPENDIX H

GRID LOCATION, OVERLAPPING, AND BOUNDARY INTERPOLATION

The two-way grid interpolation process indicated by the three asterisks on figure 1.3 is designed so that interpolated values for the lateral boundaries of a fine grid are obtained only from forecast values (as opposed to interpolated values) on the surrounding coarser grid. (Interpolation is only done at the full time step, since the half time step values in the Lax-Wendroff process are only derived quantities.) Similarly, the interior boundary values on that coarser grid (which are located near the outer boundaries of the fine grid) are renewed by interpolation from the fine grid without using the interpolated outer gridpoint data on that fine grid. These requirements set a lower limit to the amount by which the two grids "overlap." At the same time, computational efficiency requires that this overlap be small. (A largely intuitive feeling that unnecessary overlap would be detrimental also argues for minimizing the overlap.)

A critical point in deciding the minimum overlap is the number of surrounding gridpoints (on any grid) that are required to advance each of the variables H, Hu, Hv, Hθ, and Hq at one gridpoint a complete Lax-Wendroff step from t to t+Δt. A careful examination of the complete set of finite-difference equations listed in Appendixes A-G results in the three diagrams of figure H.1.[1]

The upper part of figure H.2 illustrates the effect of figure H.1 on the full time step forecast variables [denoted simply by H, V, and U in place of (H, Hθ, Hq), Hv, and Hu] along a grid row of constant j subscript (see figs. 2.1 and H.2). If all plotted variables in this diagram at time step n are available, but none are available to the left, the boundary of valid forecast data moves to the right at later time steps, as shown by the heavy curve. From this it follows that if the diagram refers to the left boundary of a fine grid (which according to fig. 1.3 is replenished every two time steps), it will be necessary to replenish at n+2 the four leftmost V values and the three leftmost U and H values by interpolation. On the other hand, if the diagram refers to a coarse grid set of variables on a j-row that intersects an inner fine grid lying to the left of the diagram, interpolation is performed every time step. Therefore, only the two leftmost V's and the single leftmost U and H shown there need be replenished in the interior of the coarse grid. Similar arguments are readily made for the loss of valid data in successive time steps at a rightmost grid boundary and at the "top" and "bottom" of a column of constant i subscript.

---

[1]The horizontal averaging used in eq (D.5)-(D.8), (G.1)-(G.5), and (G.22)-(G.25) account for the outermost influence points in this figure.

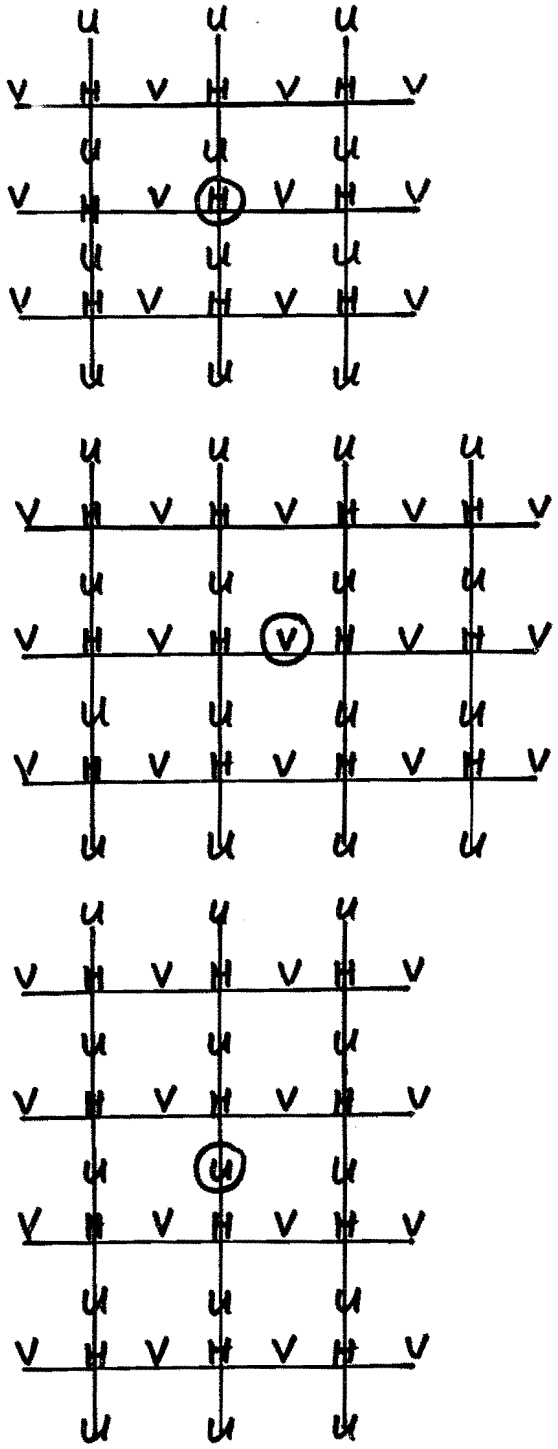

Figure H.1.--Neighboring data points needed to make one complete Lax-Wendroff time step for the central variable enclosed in a circle. The symbols H, U, V represent the full time step variables (H, Hθ, Hq), Hu, and Hv.

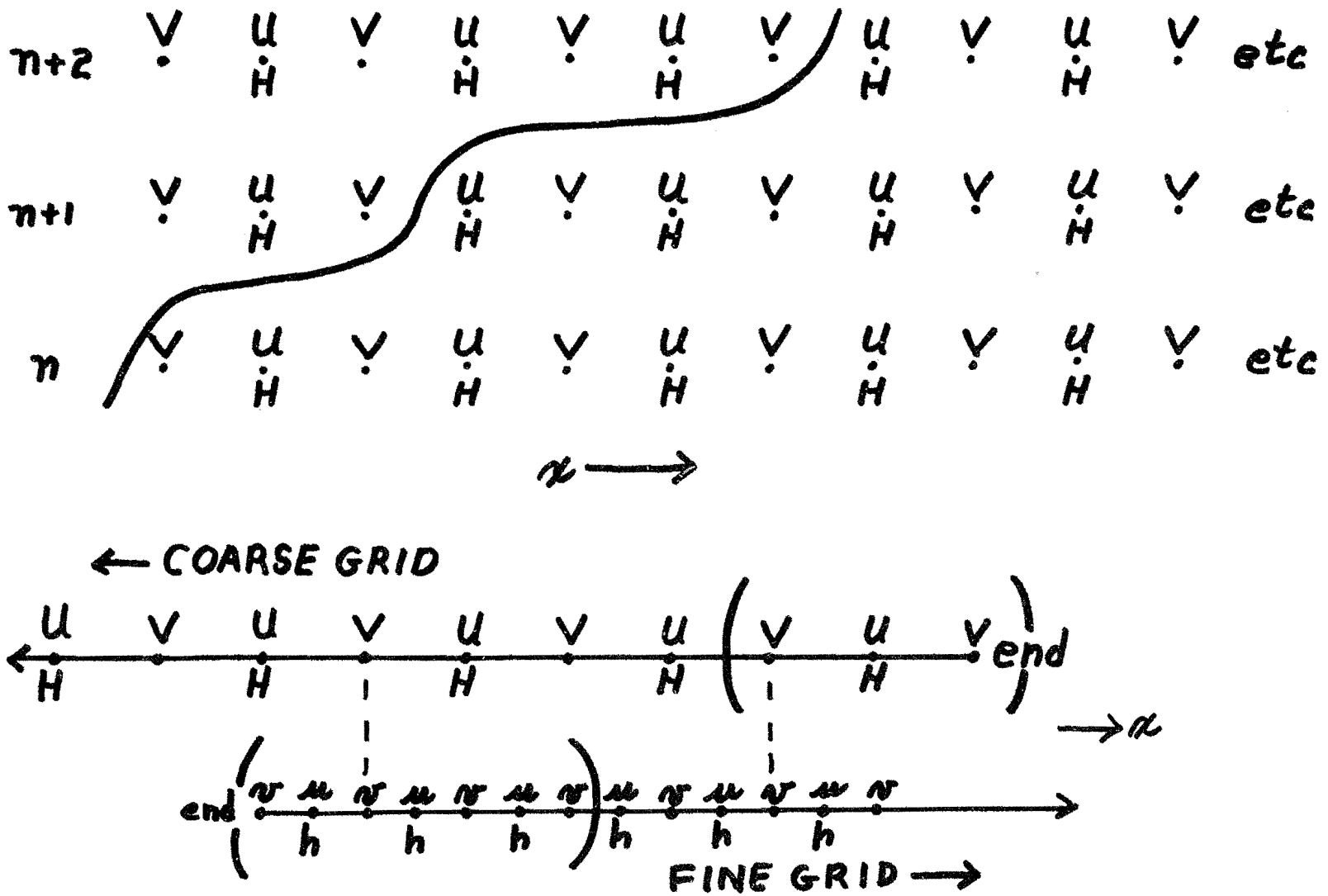

Figure H.2.--(Top) Progression to the right (+x) at successive full time steps of the left edge of valid data. (Bottom) Location of left edge of a fine grid relative to surrounding coarse grid. Variables in ( ) are interpolated from the other grid.

The interpolation process used is that of bilinear interpolation (Phillips 1962). Let i* and j* define the (noninteger) location of a point for which an interpolated value of a variable h is desired, and let this point be located in the grid square of h values identified by having i and j at its lower left corner:

$$0 \leq (i^* - i) \equiv X < 1$$
$$0 \leq (j^* - j) \equiv Y < 1. \qquad \text{(H.1)}$$

The bilinear interpolation formula for the variable h is

$$h(i^*,j^*) = (1-X)(1-Y)h_{ij} + X(1-Y)h_{i+1j} + Y(1-X)h_{ij+1} + XYh_{i+1j+1}. \qquad \text{(H.2)}$$

The lower diagram of figure H.2 can now be constructed. It shows that location (in the x-direction) of the leftmost edge of a fine grid with respect to the points of the surrounding coarse grid which minimizes the overlap, but allows the parenthesized quantities on each grid to be obtained from the other by means of eq (H.2).

These arguments can be extended to the right, top, and bottom boundaries of the fine grid, and the result is given in figure H.3. The intersections of the lines on this figure represent the (H, Hθ, Hq) points of a fine grid having $i_m = j_m = 23$. The plotted lower case characters h, u, and v show the complete set of fine grid variables (H, Hθ, Hq), HU, and HV which are obtained by interpolation from the coarse grid. The plotted upper case characters H, U, and V denote the complete set of coarse grid "internal boundary" variables (H, Hθ, Hq), HU, and HV that are obtained by interpolation from the fine grid.

On the fine grid of figure H.3, all variables interior to the interpolated (i.e., plotted) values are forecast every time step in cycle steps 1-6 of figure 3. In cycle steps 1, 3, and 4, the two innermost rings of each plotted symbol are also forecast.[1] (Figure H.3 does not show h and u values for i=1, nor h and v values for j=1. For simplicity these are "stored" in the data arrays, but are not used in the computations.)

On the coarse grid of figure H.3, a forecast is made in the cycle steps 3, 6, and 7 of figure 1.3 for all variables outside the rings of plotted H, V, U symbols on that figure (subject, of course, to any outer boundary interpolation point limitations for grid B and the equatorial conditions for grid A). In the interest of efficiency,

---

[1] All grid point values on a fine grid could be forecast, since any "junk" produced thereby at outer points is prevented by the interpolation process from contaminating the meaningful interior values. In the interest of efficiency, however, the NGM code omits making computations which are easily recognized as meaningless.

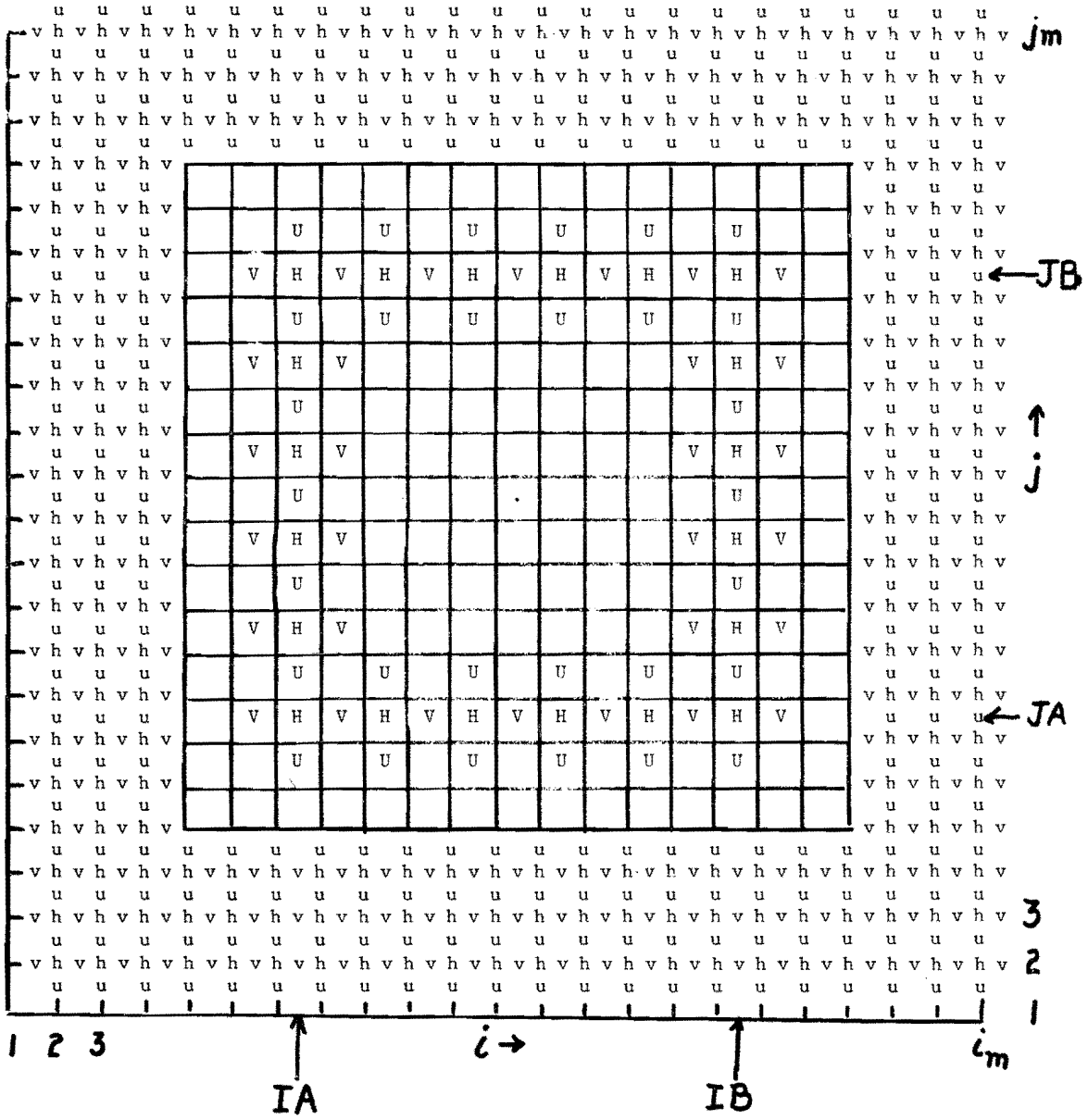

Figure H.3.--A sample fine grid. The lower case letters h, u, v show the grid points for which data is obtained every second time step by interpolation from the coarse grid. The upper case symbols are the complete set of coarse grid point values obtained by interpolation at each time step of the coarse grid.

the NGM code does not make computations in the "hole" of a coarser grid that exists whenever the next finer grid is present, such as the (unplotted) H, U, V points interior to the plotted H, U, V points on figure H.3. (This is accomplished by means of variable limits for "DO" loops on the index i and "IF" tests on the j-index. The irregular equatorial limits of the grid A forecast points (Appendix I) are also treated with variable DO loop limits on i. CPU time was reduced by about 15 percent through this special DO-loop procedure.)

The grids on figure H.3 are located so that H, U, and V of the coarse grid are each located in the center of a fine mesh H-point grid square. The i subscript assigned to the two coarse grid columns of interpolated (H,U) values and the j subscript of the two coarse grid rows of interpolated (H,V) values are identified by four numbers:

$$\text{IA, IB: JA, JB.} \tag{H.3}$$

Let the fine grid have i and j ranges

$$\begin{aligned} i &= 1, i_m \\ j &= 1, j_m. \end{aligned} \tag{H.4}$$

Both i_m and j_m must be odd integers. Let this fine grid have the North Pole coordinates (for its H points):

$$i_p, j_p. \tag{H.5}$$

(These will not be integers.) Let I_p, J_p denote the (known) pole location for the coarse grid. Then two integers,

$$\text{ISUM} = \text{IA} + \text{IB}, \tag{H.6}$$

$$\text{JSUM} = \text{JA} + \text{JB}, \tag{H.7}$$

are sufficient, given also the overall (odd) dimensions i_m, j_m of the fine grid and the pole location I_p, J_p of the coarse grid, to determine the six numbers

$$\text{IA, IB, JA, JB; } i_p, j_p \text{ .} \tag{H.8}$$

The location of the interior boundary points of the coarse grid and the location of the entire fine mesh is thereby fixed.

The arithmetic for this is as follows. (It is of course based on the ratio of 2 between the two grid resolutions.)

$$IA = (2 \cdot ISUM + 13 - i_m)/4 \tag{H.9}$$

$$IB = (2 \cdot ISUM - 13 + i_m)/4 \tag{H.10}$$

$$JA = (2 \cdot JSUM + 13 - j_m)/4 \tag{H.11}$$

$$JB = (2 \cdot JSUM - 13 + j_m)/4 \tag{H.12}$$

$$i_p = 0.5\ i_m + 1 + 2I_p - ISUM \tag{H.13}$$

$$j_p = 0.5\ j_m + 1 + 2J_p - JSUM. \tag{H.14}$$

For (H.9)-(H.12) to have integer values, ISUM must be even or odd according as $\frac{1}{2}(i_m-1)$ is even or odd, and JSUM must be even or odd according as $\frac{1}{2}(j_m-1)$ is even or odd.

Another restriction arises from the separation of JA from JB. A requirement that (IB-IA) and (JB-JA) must be at least equal to 2 leads to the restrictions

$$i_m \geq 17,\ j_m \geq 17, \tag{H.15}$$

on the horizontal dimensions of grids B and C.

IA, IB, JA, JB must also satisfy the condition that they are sufficiently removed from the outer boundaries of the coarse grid that there is a sufficiently wide ring of forecast values on the coarse grid to allow interpolation of the complete outer rings of fine mesh variables plotted on figure H.3. For grid B this leads to the following condition on its IA, IB, JA, JB values:

$$\begin{aligned} IA &\geq 9, \quad IB \leq I_m - 7 \\ JA &\geq 9, \quad JB \leq J_m - 7. \end{aligned} \tag{H.16}$$

For grid B, eq (H.16) has been of practical consequence only with respect to JA, when it has been desirable to locate the bottom row j=1 of grid C as close as possible to the bottom of grid B (so that grid C can include all of Mexico, for example).

The equivalent of eq (H.16) for grid A is more complicated, since the outer forecast boundary of grid A is not a rectangle (see Appendix I). However, the forecast gridpoints for each forecast variable on grid A extend far enough south of the Equator so that the Northern Hemisphere is completely covered by forecast grid squares for that variable. A sufficient test that all outer boundary interpolated

points of grid B (the lower case letters on figure H.3) can be obtained properly from grid A is therefore that the eight corner u and v points on that figure be in the Northern Hemisphere. The conditions are that the eight quantities: $(\ell_1^2 + \ell_2^2)$, $(\ell_3^2 + \ell_4^2)$, $(\ell_5^2 + \ell_2^2)$, $(\ell_6^2 + \ell_4^2)$, $(\ell_1^2 + \ell_7^2)$, $(\ell_3^2 + \ell_8^2)$, $(\ell_5^2 + \ell_7^2)$, $(\ell_6^2 + \ell_8^2)$ are all less than $(2NH + 1)^2$, where

$$\begin{aligned} \ell_1 &= i_p - 2 \\ \ell_2 &= j_p - 1.5 \\ \ell_3 &= i_p - 1.5 \\ \ell_4 &= j_p - 2 \\ \ell_5 &= i_m - i_p \\ \ell_6 &= i_m + .5 - i_p \\ \ell_7 &= j_m + .5 - j_p \\ \ell_8 &= j_m - j_p \end{aligned} \qquad \text{(H.17)}$$

and i_p, j_p, i_m, and j_m are the values for grid B.

The interpolation of inner boundary data at the new time step for grid A (or B) takes place as successive j-rows of grids B (or C) are forecast for the new time step during the cycle step 6 (or 2 and 5) for grid B (or C) of figure 1.3 and stored in core for later use. The interpolation of outer boundary data for grid B (or C) takes place similarly during cycle step 7 (or 3 and 6) when the surrounding coarse grid data are in core. The complete bottom rows j = 1,2,3,4 and top rows j_m-2, j_m-1, and j_m are written at once on the disk file of updated j-rows for grid B (or C), while the remaining outer boundary data on the fine grid of figure H.3 are accumulated temporarily in core in a special format. The latter outer boundary data are inserted in each appropriate j row of initial data of grids C and B after the latter are read into core during cycle steps 1, 4, and 6. The inner boundary data are similarly inserted into each j row of initial data in cycle steps 3, 6, and 7.

A dummy time cycle of the forecast code using $\Delta t = 0$ (but doing all boundary interpolations and insertions) is invoked at the beginning and end of each forecast run. This ensures that all variable arrays are completely filled out with updated boundary values.

APPENDIX I

EQUATORIAL CONDITIONS FOR GRID A

These are based on the symmetry conditions eq (1.12), but suitably transformed in the case of the stereographic velocity components eq (2.5) and (2.6). Let the subscript s define a variable desired at the point with latitude $-\theta$, longitude λ; let subscript n define the same quantity at the Northern Hemisphere "image point" with latitude $+\theta$ and longitude λ. Then the stereographic velocity components satisfy the following symmetry conditions:

$$u_s = -u_n \cos 2\lambda - v_n \sin 2\lambda, \tag{I.1}$$

$$v_s = v_n \cos 2\lambda - u_n \sin 2\lambda. \tag{I.2}$$

The even variables H, Hθ, Hq obey the simpler law

$$h_s = h_n, \tag{I.3}$$

and eq (I.1) and (I.2) therefore apply equally well to the products Hu and Hv.

A subroutine in the NGM input program examines the grid A structure defined by eq (1.5), (1.6), and (1.7) separately for the staggered H, Hu, and Hv variables of figure 2.1. It maps out for each of these variable types the collection of i,j points on grid A that forms a connected array of grid squares that minimally, but completely, cover the entire Northern Hemisphere. These define the outer limits of the grid A forecast points. After the subroutine has done this for each of H, Hu, and Hv, the three influence diagrams of figure H.1 are used to establish how far in the Southern Hemisphere beyond the above forecast domains, values of H, Hu, Hv, etc., are needed to allow a one time step forecast for the outermost forecast points. This defines a ring of grid A outer interpolation points in the Southern Hemisphere.

This results in 12 tables of i-limits giving, for each j=1,...,(2NH+6) (and each of the three variable types), the i-values for the first interpolation point, the first forecast point, the last forecast point, and the last interpolated point for that variable on that j row of grid A.

These numbers are of course useful in the forecast code, but they are also used in the final operation shown on figure 1.3, the replenishment of the outer grid points of grid A.

If i,j is a grid A interpolation point in the Southern Hemisphere, the coordinates i*,j* of its image point in the Northern Hemisphere are readily derivable from eq (1.5). For H, Hθ, and Hq these are

$$i^* = NH + 4 + \frac{(NH + .5)^2 X}{X^2 + Y^2} \tag{I.4}$$

$$j^* = NH + 4 + \frac{(NH + .5)^2 Y}{X^2 + Y^2} \tag{I.5}$$

where

$$X = i - (NH + 4), \tag{I.6}$$

$$Y = j - (NH + 4). \tag{I.7}$$

The Northern Hemisphere values on the right sides of eq (I.1)-(I.3) are then obtained by a bilinear horizontal interpolation procedure identical with eq (H.1) and (H.2). Additions of 0.5 to eq (I.6) or (I.7) and subtractions from eq (I.4) or (I.5) must be made appropriately according to the staggered locations shown in figure 2.1 when using eq (I.1) and (I.2).

This equatorial boundary procedure has been very well-behaved from a numerical point of view.

(Continued from inside front cover)

NWS 16 Storm Tide Frequencies on the South Carolina Coast. Vance A. Myers, June 1975, 79 p. (COM-75-11335)

NWS 17 Estimation of Hurricane Storm Surge in Apalachicola Bay, Florida. James E. Overland, June 1975. 66 p. (COM-75-11332)

NWS 18 Joint Probability Method of Tide Frequency Analysis Applied to Apalachicola Bay and St. George Sound, Florida. Francis P. Ho and Vance A. Myers, November 1975, 43 p. (PB-251123)

NWS 19 A Point Energy and Mass Balance Model of a Snow Cover. Eric A. Anderson, February 1976, 150 p. (PB-254653)

NWS 20 Precipitable Water Over the United States, Volume 1: Monthly Means. George A. Lott, November 1976, 173 p. (PB-264219)

NWS 21 Interduration Precipitation Relations for Storms - Southeast States. Ralph H. Frederick, March 1979, 66 p.

NOAA SCIENTIFIC AND TECHNICAL PUBLICATIONS

The National Oceanic and Atmospheric Administration was established as part of the Department of Commerce on October 3, 1970. The mission responsibilities of NOAA are to assess the socioeconomic impact of natural and technological changes in the environment and to monitor and predict the state of the solid Earth, the oceans and their living resources, the atmosphere, and the space environment of the Earth.

The major components of NOAA regularly produce various types of scientific and technical information in the following kinds of publications:

PROFESSIONAL PAPERS — Important definitive research results, major techniques, and special investigations.

CONTRACT AND GRANT REPORTS — Reports prepared by contractors or grantees under NOAA sponsorship.

ATLAS — Presentation of analyzed data generally in the form of maps showing distribution of rainfall, chemical and physical conditions of oceans and atmosphere, distribution of fishes and marine mammals, ionospheric conditions, etc.

TECHNICAL SERVICE PUBLICATIONS — Reports containing data, observations, instructions, etc. A partial listing includes data serials; prediction and outlook periodicals; technical manuals, training papers, planning reports, and information serials; and miscellaneous technical publications.

TECHNICAL REPORTS — Journal quality with extensive details, mathematical developments, or data listings.

TECHNICAL MEMORANDUMS — Reports of preliminary, partial, or negative research or technology results, interim instructions, and the like.

Information on availability of NOAA publications can be obtained from:

ENVIRONMENTAL SCIENCE INFORMATION CENTER (D822)
ENVIRONMENTAL DATA AND INFORMATION SERVICE
NATIONAL OCEANIC AND ATMOSPHERIC ADMINISTRATION
U.S. DEPARTMENT OF COMMERCE

6009 Executive Boulevard
Rockville, MD 20852

NOAA--S/T 79-41